https://doi.org/10.5194/egusphere-2026-4450
Preprint. Discussion started: 13 August 2026

Highly oxygenated organic molecule formation from 2,5-dimethylfuran oxidation by O_3 and OH: an experimental and computational study

Rabbia Asgher[1,★], Sakshi Jha[1,★], Avinash Kumar[1], Shawon Barua[1], Prasenjit Seal[1], Sana Farhoudian[1], Siddharth Iyer[1], and Matti Rissanen[1,2]

[1]Aerosol Physics Laboratory, Physics Unit, Tampere University, 33720 Tampere, Finland
[2]Department of Chemistry, University of Helsinki, 00560 Helsinki, Finland
★These authors contributed equally to this work.

Correspondence: Rabbia Asgher (rabbia.asgher@tuni.fi), Sakshi Jha (sakshi.jha@tuni.fi), and Matti Rissanen (matti.rissanen@tuni.fi)

Abstract. The gas-phase oxidation of 2,5-dimethylfuran (2,5-DMF) by ozone (O_3) and hydroxyl radicals (OH) was investigated in flow reactors at atmospheric pressure and room temperature using nitrate chemical ionization orbitrap mass spectrometry. At a residence time of 0.8 s, highly oxygenated organic molecules (HOM) with up to nine oxygen atoms were detected in the ozonolysis channel, and eight oxygen atoms in the OH channel. These observations demonstrate that sequential intramolecular hydrogen-shift autoxidation is sufficiently rapid to form products with up to nine oxygen atoms on sub-second timescales. At 7 s, C_{10}–C_{12} accretion products form through different combinations of C_5 and C_6 alkyl peroxy (RO_2) radicals. Quantum chemical calculations using density functional theory and coupled-cluster methods identified a distinct Criegee intermediate geometry (Anti-CI-2A) that provides a plausible route to HOM species containing up to nine oxygen atoms. Its different methyl/hydrogen orientation relative to the conventional Syn and Anti conformers enables a rapid 1,6-H shift, facilitating autoxidation toward O_9 formation and suggesting that primary ozonide decomposition in structurally complex ozonolysis systems may access reactive Criegee intermediate geometries beyond the conventional Syn and Anti forms. For OH-initiated oxidation, the proposed mechanism accounts for HOM monomer formation up to O_6, with rapid termination and radical recycling limiting further autoxidation. Overall, 2,5-DMF produces low-volatility oxidation products from both ozonolysis and OH-initiated pathways with implications for secondary organic aerosol formation.

1 Introduction

Secondary organic aerosol (SOA) formation from the atmospheric oxidation of biogenic and pyrogenic volatile organic compounds (VOC) constitutes a major uncertainty in assessments of aerosol radiative forcing and air quality (Jimenez et al., 2009; Hallquist et al., 2009). Furans and alkylated furans are emitted into the atmosphere primarily through biomass burning, with additional contributions from secondary gas-phase oxidation of isoprene and related dienes (Gilman et al., 2015; Koss et al., 2018; Andreae, 2019; Atkinson and Arey, 2003; Romanias et al., 2024). Among these species, 2,5-dimethylfuran (2,5-DMF) serves as a tracer of biomass burning and indoor combustion emissions (Fu et al., 2021). It is also a biomass-derived biofuel

https://doi.org/10.5194/egusphere-2026-4450
Preprint. Discussion started: 13 August 2026

candidate (Román-Leshkov et al., 2007; Qian et al., 2015; Hoang et al., 2022), and incomplete combustion and evaporative losses from its use constitute an additional atmospheric emission source. OH radicals, O_3, and NO_3 radicals remove 2,5-DMF from the atmosphere through mechanistically distinct oxidation pathways (Cabañas et al., 2004; Matsumoto, 2011; Whelan et al., 2020; Newland et al., 2021). Each channel generates peroxy radical intermediates whose subsequent chemistry determines the formation of low-volatility oxidation products.

Unlike fully aromatic compounds such as benzene, which resist electrophilic addition by O_3 due to complete π delocalization, 2,5-DMF undergoes efficient ozonolysis. Initial O_3 attack proceeds via 1,3-cycloaddition across the C2=C3 bond of the furan ring (Fig. 1a), forming a chemically activated primary ozonide (POZ) that decomposes promptly to *syn* and *anti* Criegee intermediates. *Syn*-CI undergoes a 1,4-H shift to form a vinyl hydroperoxide (VHP), which decomposes to release OH and form a carbon-centred radical. The radical adds O_2 to form the ozonolysis-derived RO_2, which retains an ether-linked oxygen from the opened furan ring (Johnson and Marston, 2008; Vereecken et al., 2015; Li et al., 2018; Illmann and Rösgen, 2024; Yu et al., 2025).

OH reacts with 2,5-DMF via addition to the furan ring at the C2 or C3 positions (Fig. 1b), producing structurally distinct ring-retaining hydroxyalkyl radicals, or via H-abstraction from the methyl substituents, generating methylenefuranyl radicals (Atkinson and Arey, 2003; Aschmann et al., 2011; Jiang et al., 2020). Both ring-addition isomers add O_2 to form RO_2 radicals differing in the relative configuration of the hydroxyl and peroxy groups; H-abstraction produces a structurally and compositionally distinct RO_2. These three RO_2 populations differ in ring-opening rate, oxygenation pattern, and available H-shift sites. The distinct initiation mechanisms and resulting RO_2 structures are summarized schematically in Fig. 1.

https://doi.org/10.5194/egusphere-2026-4450
Preprint. Discussion started: 13 August 2026

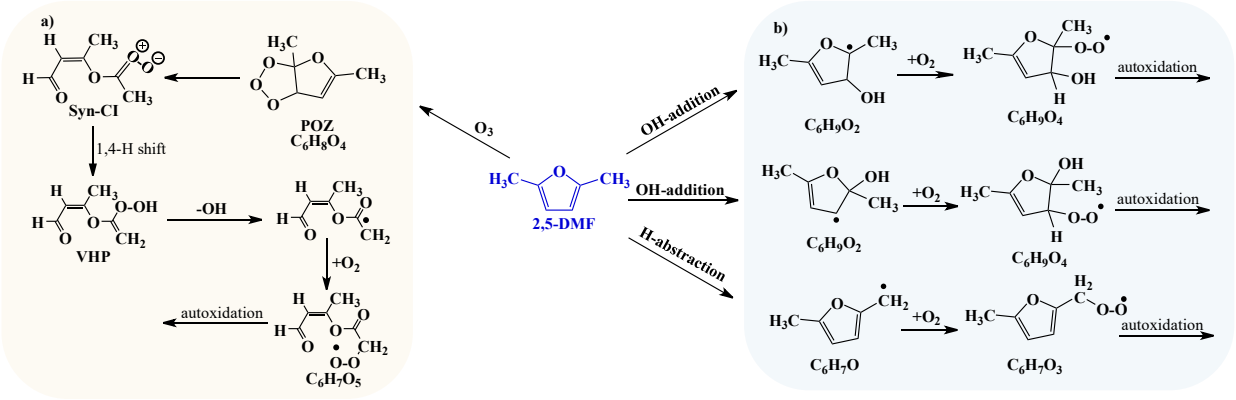

Figure 1. Oxidation initiation pathways of 2,5-DMF by (a) O_3 and (b) OH. (a) O_3 adds across the C2=C3 bond via 1,3-cycloaddition to form the primary ozonide (POZ, $C_6H_8O_4$), which decomposes to Criegee intermediates. The *syn*-CI-1 conformer undergoes a 1,4-H shift to form a vinyl hydroperoxide (VHP) that releases OH, yielding a carbon-centred radical. Subsequent O_2 addition produces the acyclic peroxy radical $C_6H_7O_5$, which undergoes sequential intramolecular H-shift autoxidation. (b) OH addition to the furan ring at the C2 or C3 position produces ring-retaining $C_6H_9O_2$ radicals, and H-abstraction from the methyl substituent produces a ring-retaining methylenefuranyl radical (C_6H_7O). O_2 addition yields the peroxy radicals $C_6H_9O_4$ (ring-addition) or $C_6H_7O_3$ (H-abstraction), both of which undergo autoxidation.

The fate of RO_2 radicals formed in both systems is governed by competition between intramolecular hydrogen-shift isomerization and bimolecular loss via $RO_2 + HO_2$ and $RO_2 + RO_2$ reactions. When intramolecular H-shift rate coefficients exceed the effective bimolecular RO_2 sink, sequential oxygen addition propagates and produces highly oxygenated peroxy intermediates — a process termed autoxidation (Vereecken et al., 2007; Crounse et al., 2013; Ehn et al., 2014; Jokinen et al., 2014; Rissanen et al., 2014). Autoxidation generates highly oxygenated organic molecules (HOM) comprising a dominant fraction of the lowest-volatility condensable organics in monoterpene and aromatic oxidation systems (Ehn et al., 2014; Garmash et al., 2020; Iyer et al., 2023). The efficiency of this process is strongly modulated by molecular structure: H-shift rate coefficients increase systematically with the number of abstractable hydrogen atoms in geometrically favourable positions and decrease when ring constraints restrict conformational access to viable transition states (Otkjær et al., 2018; Møller et al., 2020). Fully aromatic rings resist electrophilic addition because complete π delocalization stabilizes the ring against disruption (Atkinson and Carter, 1984). The furan ring, however, has substantially weaker aromaticity than benzene. Oxidant addition to the furan C=C bond disrupts the π system, generating a non-aromatic intermediate whose unimolecular chemistry proceeds orders of magnitude faster than in fully aromatic systems (Atkinson et al., 1983; Matsumoto, 2011; Illmann and Rösgen, 2024). An analogous ring-opening requirement operates in toluene, where the bicyclic peroxy radical undergoes molecular rearrangement which leads to a ring-broken RO_2 before autoxidation proceeds on sub-second timescales (Iyer et al., 2023). In the 2,5-DMF system, ozonolysis opens the furan ring during CI formation, so the resulting RO_2 radical is already acyclic. Conversely, OH addition retains the ring initially but generates a hydroxyl-substituted RO_2 with methyl groups that provide additional ab-

https://doi.org/10.5194/egusphere-2026-4450
Preprint. Discussion started: 13 August 2026

stractable H atoms due to allylic resonance stabilization of the abstraction transition state. Whether these structural differences translate into efficient autoxidation has not been experimentally constrained.

Several studies have characterized the OH-initiated oxidation of 2,5-DMF. Early rate coefficient measurements established high OH reactivity (Bierbach et al., 1992). Relative-rate experiments subsequently reported $k(\mathrm{OH} + 2,5\text{-DMF}) = (12.5 \pm 0.4) \times 10^{-11}\,\mathrm{cm^3\,molecule^{-1}\,s^{-1}}$ and identified 3-hexene-2,5-dione as the major first-generation carbonyl product, at molar yields of $24 \pm 3\,\%$ in the presence of NO and $34 \pm 3\,\%$ in its absence (Aschmann et al., 2011). Quantum chemical and RRKM-ME calculations resolved the first-generation $\mathrm{RO_2}$ branching for 2,5-DMF at 298 K and 760 Torr, predicting that a minor fraction (0.28) undergoes ring opening to form 3-hexene-2,5-dione, while the dominant pathway yields ring-retaining adducts at the C2/C5 positions (Yuan et al., 2017). Absolute rate coefficient measurements by pulsed laser photolysis–laser-induced fluorescence subsequently confirmed rapid OH addition across a wide temperature and pressure range (Whelan et al., 2020). Collectively, these studies establish the dominant removal pathway, primary carbonyl formation channel, and first-generation $\mathrm{RO_2}$ structure, but none constrains whether the initial $\mathrm{RO_2}$ radicals undergo sequential intramolecular H-shift autoxidation.

The ozonolysis of 2,5-DMF has been investigated by flow tube kinetics and atmospheric simulation chamber experiments. Matsumoto (2011) determined $k(\mathrm{O_3} + 2,5\text{-DMF}) = (4.2 \pm 0.9) \times 10^{-16}\,\mathrm{cm^3\,molecule^{-1}\,s^{-1}}$ at 295 K using a coaxial glass flow tube reactor with reaction times of 27–50 s. This rate coefficient is five times greater than that of α-pinene ($k \approx 8.4 \times 10^{-17}\,\mathrm{cm^3\,molecule^{-1}\,s^{-1}}$; Atkinson and Arey 2003), placing 2,5-DMF ozonolysis on an atmospherically relevant timescale alongside established monoterpene sources of $\mathrm{RO_2}$. Quantum chemical calculations at the CCSD(T)-F12a//M06-2X level reproduced this rate enhancement across the furan series and showed that POZ decomposition proceeds almost exclusively through the *syn* and *anti* conformers of the dominant Criegee intermediate, which together account for a combined fractional yield of 0.95 (Li et al., 2018). Illmann and Rösgen (2024) subsequently characterised the product distribution from 2,5-DMF ozonolysis in the QUAREC atmospheric simulation chamber at (299 ± 2) K and (980 ± 20) hPa over reaction timescales of tens of minutes, monitoring the gas phase by long-path FTIR spectroscopy and PTR-ToF-MS. They reported $k(\mathrm{O_3} + 2,5\text{-DMF}) = (3.3 \pm 1.0) \times 10^{-16}\,\mathrm{cm^3\,molecule^{-1}\,s^{-1}}$, in agreement with Matsumoto (2011), and identified formaldehyde ($\mathrm{CH_2O}$), methyl glyoxal ($\mathrm{C_3H_4O_2}$), ketene ($\mathrm{C_2H_2O}$), glyoxal ($\mathrm{C_2H_2O_2}$), methyl hydroperoxide ($\mathrm{CH_4O_2}$), acetic anhydride ($\mathrm{C_4H_6O_3}$), and acetic acid ($\mathrm{C_2H_4O_2}$) as first-generation products. The total carbon balance remained below $50\,\%$, indicating that a substantial fraction of reacted carbon partitions into low-volatility products undetectable by FTIR and PTR-ToF-MS. An OH yield of at most $(25 \pm 10)\,\%$ was inferred using 1,3,5-trimethylbenzene as an OH tracer, confirming that ozonolysis experiments without explicit OH scavenging represent a mixed $\mathrm{O_3}$ and *in situ* OH oxidation system. Illmann and Rösgen (2024) identified a 1,4-H shift isomerization of the carbonyl-substituted peroxy radical DICARBO2, formed from the dominant Z-CI1 pathway, as competitive with bimolecular $\mathrm{RO_2}$ loss under their experimental conditions, providing the first experimental evidence of unimolecular $\mathrm{RO_2}$ isomerization in this system. Tajuelo et al. (2021) observed that 2,5-DMF ozonolysis generates new particles only in the presence of $\mathrm{SO_2}$ at (296 ± 1) K, and whether condensation onto pre-existing seed aerosol would yield SOA in its absence remains untested. Collectively, these studies constrain the primary low-molecular-weight product distribution at reaction timescales of tens of seconds to minutes, but leave unaddressed whether $\mathrm{O_3}$-derived $\mathrm{RO_2}$ radicals

https://doi.org/10.5194/egusphere-2026-4450
Preprint. Discussion started: 13 August 2026

undergo intramolecular H-shift isomerization sufficiently rapid to sustain sequential oxygen addition against bimolecular loss at sub-second timescales.

In this work, the gas-phase oxidation of 2,5-DMF is investigated in borosilicate glass flow reactors at residence times of 0.8 s and 7 s. The shorter residence time targets the autoxidation-dominated regime before bimolecular RO_2 reactions become competitive, while the longer residence time captures conditions where unimolecular autoxidation and bimolecular RO_2 pathways contribute concurrently and accretion products formed through RO_2 + RO_2 cross-reactions become observable. This dual-timescale approach provides direct access to nascent RO_2 intermediates on sub-second timescales and targets the $>50\,\%$ unaccounted carbon fraction identified by Illmann and Rösgen (2024). Both ozonolysis and OH-initiated pathways are examined, with selective suppression of the OH channel by CO scavenging enabling mechanistic separation of the two oxidant contributions. Oxidation products are detected by chemical ionization mass spectrometry. Experimental observations are complemented by quantum chemical calculations constraining key reaction pathways and rate-limiting steps in HOM formation.

2 Methods

2.1 Experimental method

Gas-phase oxidation of 2,5-DMF by O_3 and OH was investigated in borosilicate glass flow reactors at atmospheric pressure and room temperature, with oxidation products detected using an Orbitrap mass spectrometer (Exploris 240, Thermo Fisher Scientific) equipped with a multi-scheme chemical ionization inlet (MION; Karsa Oy; Rissanen et al., 2019; He et al., 2023), operated with NO_3^- chemical ionization (Jokinen et al., 2012; Hyttinen et al., 2015). Two flow reactors, operated at atmospheric pressure and room temperature, provided complementary residence times: a short-residence-time reactor (inner diameter 2.2 cm, length 47 cm, total flow 12.8 slpm, $\Delta t = 0.8$ s) and a long-residence-time reactor (inner diameter 4.7 cm, length 100 cm, total inlet flow 15.8 slpm, $\Delta t = 7$ s). Purified zero air (Aadco 737) served as the carrier gas, and all reactant and oxidant flows were regulated by calibrated mass flow controllers (Alicat Scientific Inc.). Ozone was generated by 185 nm photolysis of zero air using a pen-ray mercury lamp (UVP, Analytik Jena). OH radicals were generated in situ via vinyl hydroperoxide (VHP) decomposition during 2,5-DMF ozonolysis, and additionally, in selected experiments, via ozonolysis of tetramethylethylene (TME; C_6H_{12}). 2,5-DMF was supplied to the flow tube reactor from a premixed cylinder (134 ppmv in N_2). Further details of experimental conditions are summarized in Table 1, and chemical purities and gas cylinder specifications are provided in Sect. S2 in the Supplement. The experimental setup is shown schematically in Fig. S1 in the Supplement.

https://doi.org/10.5194/egusphere-2026-4450
Preprint. Discussion started: 13 August 2026

Table 1. Experimental conditions for 2,5-dimethylfuran (2,5-DMF) oxidation experiments.

	Reactant concentration (ppb)				Additives[b]	
Experiment	[2,5-DMF]	[O_3]	[TME]	[NO]	D_2O	CO
Short residence time ($\Delta t^a = 0.8\,s$)						
O_3 only	105–1360	20–165	–	–	–	–
O_3 + TME (ext. OH[c])	105–1360	20–165	25–100	–	–	–
Extended residence time ($\Delta t^a = 7\,s$)						
O_3 only	50–848	15–115	–	–	–	–
O_3 + TME (ext. OH[c])	50–848	15–115	20–80	–	–	–
O_3 + NO	170	54	–	20–500	–	–
O_3 + TME + NO	170	54	20	20–500	–	–
Diagnostic experiments ($\Delta t^a = 7\,s$)						
H/D exchange	254	114	–	–	✓	–
H/D exchange + TME (ext. OH[c])	254	114	20	–	✓	–
CO scavenger (OH suppression)	848	114	–	–	–	✓

[a] Residence time. [b] ✓ = added; – = not used. [c] Ext. OH = OH produced via ozonolysis of tetramethylethylene (TME).

To evaluate the competition between $RO_2 + NO$ reactions and unimolecular autoxidation, nitric oxide (NO) was introduced at 20–500 ppbv, using organonitrate formation as a diagnostic for RO_2 interception. Carbon monoxide (CO) served as a selective scavenger ($CO + OH \rightarrow CO_2 + HO_2$) to suppress the OH radicals formed during 2,5-DMF ozonolysis while keeping the primary ozonolysis channel intact. This suppression simultaneously elevated HO_2 concentrations, shifting RO_2 termination toward hydroperoxide (ROOH) formation via $RO_2 + HO_2 \rightarrow ROOH + O_2$. Finally, hydrogen–deuterium (H/D) exchange experiments using D_2O vapor were performed for molecular structure elucidation. This allowed for the quantification of labile hydrogen atoms ($-OH$ and $-OOH$ groups), thereby providing a direct constraint on the number of intramolecular H-shift steps occurring during autoxidation.

2.2 Computational method

Systematic conformational sampling of all species, including reactants, transition states (TSs), intermediates, and products, was carried out to identify energetically favorable conformers using the Merck Molecular Force Field (MMFF) implemented in Spartan'24 (Wavefunction, Inc., 2024; Møller et al., 2016). The generated conformers were subsequently optimized using density functional theory (DFT). All initial conformer geometries were first optimized at the M06-2X/6-31+G(d) level, and those within 2 kcal mol^{-1} of the global minimum were subsequently re-optimized at the M06-2X/aug-cc-pVTZ level. All DFT calculations were performed using Gaussian 16 (Frisch et al., 2016).

https://doi.org/10.5194/egusphere-2026-4450
Preprint. Discussion started: 13 August 2026

For transition states, initial geometries were generated by optimizing structures with constrained forming and breaking bond distances to guide the system toward a first-order saddle point. The constraints were then removed, and the TSs were optimized at the M06-2X/6-31+G(d) level. A similar conformational sampling protocol was applied to obtain TS conformers, and those within 2 kcal mol^{-1} of the lowest-energy TS conformer were subsequently re-optimized at the M06-2X/aug-cc-pVTZ level of theory. To obtain accurate electronic energies, single-point calculations at the R(O)CCSD(T)-F12a/VDZ-F12 level of theory were performed on the lowest-energy geometries of all species using Molpro 2024.3 (Werner et al., 2024).

Rate coefficients (k), defined by Eq. (1), for the bimolecular reactions of 2,5-DMF with O_3, OH addition to 2,5-DMF, and OH-initiated H-abstraction were calculated using lowest-conformer transition state theory (LC-TST), in which only the lowest-energy conformers of both the reactants and the corresponding transition states were considered:

$$k = \sigma\kappa \frac{k_B T}{hc^\circ} \frac{Q_{TS}}{Q_{O_3/OH} Q_{2,5-DMF}} \exp\left(-\frac{E_{TS} - E_R}{k_B T}\right) \quad (1)$$

In Eq. (1), $E_{TS} - E_R$ represents the zero-point-energy-corrected (ZPE-corrected) barrier height, calculated using the lowest-energy conformers of the transition state and reactant. Q_{TS}, $Q_{O_3/OH}$, and $Q_{2,5-DMF}$ denote the total molecular partition functions of the transition state, ozone/OH radical, and 2,5-DMF, respectively. The standard concentration c° was taken as 2.46×10^{19} molecules cm^{-3}. k_B and h are the Boltzmann and Planck constants, respectively, and the temperature was fixed at 298.15 K. The symmetry factor (σ) was set to 2, reflecting the symmetric nature of 2,5-DMF, which contains two equivalent C=C double bonds that can undergo O_3 and OH addition through indistinguishable reactive pathways (Castañeda et al., 2012). The tunneling correction factor (κ) was set to 1, as both O_3 and OH addition reactions involve heavy-atom motion for which quantum tunneling is expected to be negligible (Møller et al., 2016).

Unimolecular reactions, including H-shifts, ring-opening, and ring-closing processes, were treated using multi-conformer transition state theory (MC-TST). Rate coefficients were determined by accounting for the contributions of multiple low-energy conformers according to Eq. (2):

$$k = \kappa \frac{k_B T}{h} \frac{\sum_i^{TS} \exp\left(-\frac{\Delta E_i}{k_B T}\right) Q_{TS,i}}{\sum_j^{R} \exp\left(-\frac{\Delta E_j}{k_B T}\right) Q_{R,j}} \exp\left(-\frac{E_{TS} - E_R}{k_B T}\right) \quad (2)$$

where ΔE_i is the ZPE-corrected energy of TS conformer i relative to the lowest-energy TS conformer, and $Q_{TS,i}$ is its partition function. Similarly, ΔE_j and $Q_{R,j}$ correspond to the energy and partition function of reactant conformer j, respectively. Partition functions were calculated at the M06-2X/aug-cc-pVTZ level of theory, while the final energies ($E_{TS} - E_R$) included coupled-cluster energy corrections. The tunneling correction factor κ was computed using a one-dimensional Eckart potential based on the reactant and product minima connected to the lowest-energy TS. These wells were identified through forward and reverse intrinsic reaction coordinate (IRC) calculations, with endpoint geometries optimized at the M06-2X/6-31+G(d) level, subsequently refined at the M06-2X/aug-cc-pVTZ level, and corrected using R(O)CCSD(T)-F12a/VDZ-F12 single-point energies.

https://doi.org/10.5194/egusphere-2026-4450
Preprint. Discussion started: 13 August 2026

To characterize the electronic structure of the species involved in the rate coefficient calculations, coupled-cluster T_1 diagnostic values were evaluated for the key intermediates and transition states. While the POZ dissociation transition states remained within the conventional single-reference regime ($T_1 \leq 0.02$), the Criegee intermediates, O_5–O_9 oxygenated intermediates, and their associated transition structures exhibited T_1 diagnostic values between 0.02 and 0.03 (coupled-cluster output files deposited in the Zenodo repository). In line with previous studies, these systems were treated within a single-reference framework while acknowledging the possible uncertainty associated with multireference effects (Vereecken et al., 2015; Li et al., 2023; Durán et al., 2025; Bruce and Li, 2023). Furthermore, the calculated reaction kinetics and product formation pathways were found to be consistent with the available experimental observations.

Master-equation simulations were performed using the Master Equation Solver for Multi-Energy Well Reactions (MESMER) to determine branching ratios for the decomposition of the chemically activated POZ formed in the reaction of 2,5-DMF with O_3 (Glowacki et al., 2012). POZ formation and subsequent unimolecular decomposition to two Criegee intermediates (CI-1 and CI-2) were represented in the MESMER reaction scheme using concentrations corresponding to the experimental conditions. The POZ $\rightarrow$ CI-1 and POZ $\rightarrow$ CI-2 steps were treated within the master-equation framework, with microcanonical rate coefficients calculated using the SimpleRRKM formalism with Eckart tunneling. All modeled intermediates (POZ, CI-1, and CI-2) were assigned Lennard–Jones parameters of $\sigma = 6.25$ Å and $\varepsilon = 343$ K (Hippler et al., 1983). Collisional energy transfer in N_2 bath gas was described using an exponential-down model with $\langle \Delta E \rangle_{\mathrm{down}} = 225$ cm^{-1}. An energy grain size of 100 cm^{-1} and an energy range of $50 k_{\mathrm{B}} T$ were employed. Simulations were performed at 298 K and 1 atm. The complete MESMER input file is provided in the Zenodo repository.

To gain further insight into the time evolution of HOM formation following POZ decomposition, kinetic simulations were performed using Kinetiscope (version 1.1.1328.x64) with the rate coefficients calculated in this work (Hinsberg and Houle, 2022). Simulations were conducted using a single-reactor model at constant volume, pressure, and temperature (298.15 K). To ensure adequate sampling of reaction pathways, a total particle number of 1×10^8 was used, enabling the detection of pathways that may be missed at lower particle numbers. Given the stochastic nature of Kinetiscope, multiple random seeds (28224, 11752, 26138, 11284, and 21542) were employed to assess stochastic variability and its influence on the overall kinetic behavior (Gillespie, 1976). Simulations were run for 7 s using the experimental concentrations (1360 ppbv 2,5-DMF and 117 ppbv O_3, corresponding to the short residence-time experiment of 0.8 s).

3 Results and discussion

3.1 Product distribution across sub-second and extended residence times

We examined HOM formation from 2,5-DMF oxidation at two residence times, $\Delta t = 0.8$ s and $\Delta t = 7$ s, to separate the autoxidation-dominated regime from conditions under which bimolecular RO_2 termination and accretion product formation become significant. The two oxidant channels, OH and O_3, produce structurally distinct RO_2 radicals that differ by two hydrogen atoms, generating two separable product families detectable by NO_3^- CIMS (Fig. 1). Ozonolysis opens the furan ring and, following OH elimination from the VHP, generates $C_6H_7O_5$ as the first RO_2 entering the autoxidation chain (Fig. 1a);

https://doi.org/10.5194/egusphere-2026-4450
Preprint. Discussion started: 13 August 2026

OH ring-addition produces $C_6H_9O_4$ (Fig. 1b). The two-hydrogen mass difference between these product families—$C_6H_7O_x$ and $C_6H_9O_x$—produces non-overlapping nominal masses in the NO_3^- CIMS spectrum, enabling unambiguous assignment of detected signals to the ozonolysis or OH-initiated channel, respectively. OH-initiated H-abstraction from the methyl groups also produces $C_6H_7O_x$-formula RO_2 radicals, creating a compositional overlap with the ozonolysis channel; CO scavenging resolves this ambiguity (see discussion below).

Ozonolysis generates OH in situ through VHP decomposition, with an OH yield of $25 \pm 10\,\%$ established for 2,5-DMF (Illmann and Rösgen, 2024). This OH reacts with 2,5-DMF to initiate a secondary oxidation cycle. The O_3-initiated system therefore sustains three coupled radical channels: direct ozonolysis autoxidation producing $C_6H_7O_x$, in situ OH-driven ring addition producing $C_6H_9O_x$, and an OH-initiated H-abstraction pathway that also populates the $C_6H_7O_x$ channel.

At $\Delta t = 0.8\,\mathrm{s}$, the NO_3^- CIMS spectrum demonstrates that intramolecular H-shift autoxidation proceeds via both channels (Fig. 2a; Table 2). POZ decomposition generates CI, which yields VHP ($C_6H_8O_4$). OH elimination from VHP produces the $C_6H_7O_3$ alkyl radical, which adds O_2 to form $C_6H_7O_5$; sequential H-shift and O_2 addition steps then yield $C_6H_7O_7$ and $C_6H_7O_9$. Both are detected at low intensity at $\Delta t = 0.8\,\mathrm{s}$ (Fig. 2a) and increase markedly by $\Delta t = 7\,\mathrm{s}$. OH radicals released from VHP decomposition add to the furan ring to generate $C_6H_9O_4$, and sequential H-shift and O_2 addition steps yield $C_6H_9O_6$ and $C_6H_9O_8$. Formation of $C_6H_9O_8$ requires at least two sequential H-shift/O_2 addition steps within 0.8 s, demonstrating that H-shift rate coefficients in the $C_6H_9O_4$ autoxidation chain are sufficient to compete with bimolecular RO_2 loss on sub-second timescales. The $C_5H_7O_{6\text{–}7}$ fragment signals indicate that bimolecular $RO_2 + RO_2$ termination generates RO radicals at $\Delta t = 0.8\,\mathrm{s}$. C_5 products arise from subsequent β-scission of the C_6 skeleton, with a contribution from CO loss via aldehydic fragmentation, and their detection confirms that RO_2 concentrations are sufficient for bimolecular reactions to proceed alongside autoxidation at this residence time. $C_4H_{3\text{–}6}O_6$ compositions are also detected; their formation pathways remain to be established.

https://doi.org/10.5194/egusphere-2026-4450
Preprint. Discussion started: 13 August 2026

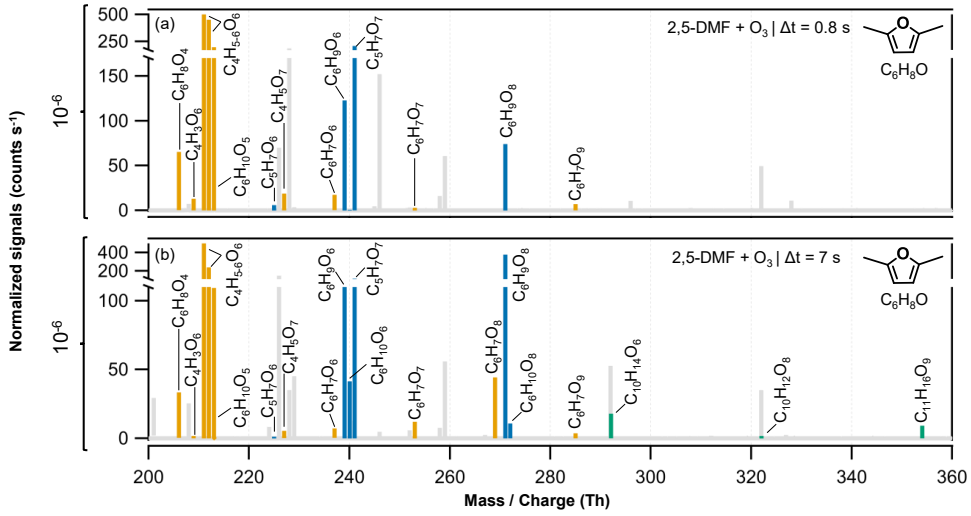

Figure 2. NO_3^- CIMS mass spectra of 2,5-DMF ozonolysis at a residence time of (a) 0.8 s: [2,5-DMF] = 1046 ppbv, $[O_3]$ = 117 ppbv; and (b) 7 s: [2,5-DMF] = 169 ppbv, $[O_3]$ = 54 ppbv. Peak labels indicate assigned neutral molecular compositions (NO_3^- adduct excluded). O_3-derived monomers ($C_6H_7O_x$) are shown in yellow, OH-derived monomers ($C_6H_9O_x$) in blue, and accretion products in green.

Table 2. Chemical compositions and $[MNO_3^-]$ adduct m/z values of oxidation products observed from 2,5-DMF ozonolysis and OH-initiated oxidation, classified by carbon skeleton and oxygenation class.

O_3-derived products			OH-derived products		
Type	Formula	m/z (Th)	Type	Formula	m/z (Th)
Intermediate[a]	$C_6H_8O_4$	206.0306	HOM O_6	$C_6H_9O_6$	239.0280
Fragment	$C_4H_3O_6$	208.9813	ROOH O_6	$C_6H_{10}O_6$	240.0359
Fragment	$C_4H_5O_6$	210.9970	Fragment	$C_5H_7O_7$	241.0073
Fragment	$C_4H_6O_6$	212.0048	HOM O_8	$C_6H_9O_8$	271.0178
Fragment	$C_4H_5O_7$	226.9918	ROOH O_8	$C_6H_{10}O_8$	272.0256
HOM O_6	$C_6H_7O_6$	237.0124	Accretion	$C_{10}H_{14}O_6$	292.0671
HOM O_7	$C_6H_7O_7$	253.0082	Accretion	$C_{10}H_{12}O_8$	322.0412
HOM O_8	$C_6H_7O_8$	269.0022	Accretion	$C_{10}H_{14}O_9$	340.0512
HOM O_9	$C_6H_7O_9$	284.9971	Accretion	$C_{12}H_{18}O_8$	352.0876
			Accretion	$C_{11}H_{16}O_9$	354.0669

m/z values correspond to $[MNO_3^-]$ adduct ions; neutral molecular compositions are listed.
[a] Primary ozonide (POZ) and its Criegee intermediate decomposition products prior to OH loss. ROOH: closed-shell $RO_2 + HO_2$ termination product. HOM O_n: highly oxygenated organic molecule with n oxygen atoms. Accretion: bimolecular $RO_2 + RO_2$ recombination product.

https://doi.org/10.5194/egusphere-2026-4450
Preprint. Discussion started: 13 August 2026

Extending the residence time to $\Delta t = 7$ s reveals a substantial shift in the product distribution toward OH-derived products (Fig. 2b). $C_6H_9O_8$ is the most intense HOM monomer signal and $C_6H_9O_6$ the second most intense, while the ozonolysis-derived $C_6H_7O_7$ and $C_6H_7O_9$ are also present at lower intensity. This shift reflects two residence-time-dependent effects: greater in situ OH formation increases $C_6H_9O_x$ signal intensities as O_3 turnover and OH yield increase with Δt, and the higher RO_2 concentrations at longer Δt shift the competition from unimolecular autoxidation toward bimolecular termination and fragmentation. The prominent closed-shell $RO_2 + HO_2$ termination products $C_6H_{10}O_6$ and $C_6H_{10}O_8$, and the elevated $C_5H_7O_7$ signal, confirm the increased bimolecular reaction flux. The larger $RO_2 + RO_2$ rate at $\Delta t = 7$ s drives $RO_2 \rightarrow RO$ conversion at a higher rate, generating alkoxy radicals that subsequently undergo CO loss and β-scission of the C_6 carbon chain.

Accretion products in the C_{10}–C_{11} range, including $C_{10}H_{14}O_{6\text{–}9}$, $C_{10}H_{12}O_8$, and $C_{11}H_{16}O_9$ (Table 2; Fig. 2b), appear at $\Delta t = 7$ s but remain below the detection limit at $\Delta t = 0.8$ s. $RO_2 + RO_2$ reactions proceed through a transient $RO\cdots OR'$ alkoxy radical complex (Valiev et al., 2019; Peräkylä et al., 2023), and the fate of this complex determines the product distribution. $C_{11}H_{16}O_9$ forms when one subunit undergoes β-scission followed by CO loss from a ring-opened alkoxy radical, reducing the carbon count from C_6 to C_5 during recombination with an intact $C_6H_9O_6$ peroxy radical. The C_{10} compositions ($C_{10}H_{12}O_8$ and $C_{10}H_{14}O_{6\text{–}9}$) require a two-carbon loss relative to direct $C_6 + C_6$ recombination and originate from the fragmentation during cross-recombination. The multiplicity of competing ring-cleavage and carbon-loss pathways precludes assignment of a single formation route from these mass spectrometric data alone. Fragmentation and accretion are therefore mechanistically coupled within the transient alkoxy complex, and both pathways intensify as $RO_2 + RO_2$ processing scales with reactor residence time.

Addition of CO as a selective OH scavenger ($CO + OH \rightarrow CO_2 + HO_2$) suppresses OH-initiated chemistry while leaving ozonolysis unaffected. This reaction simultaneously elevates HO_2 concentrations, shifting RO_2 bimolecular termination toward ROOH formation ($RO_2 + HO_2 \rightarrow ROOH + O_2$) and consequently reducing accretion product formation. The increase in HO_2 also shifts monomer RO_2 termination toward closed-shell ROOH products ($C_6H_{10}O_x$), increasing their signal intensity relative to the unperturbed experiment. Upon CO addition, $C_6H_9O_x$ signals are strongly attenuated and accretion products are nearly completely suppressed, while $C_6H_7O_x$ signals remain clearly detectable (Fig. S2). This confirms that $C_6H_9O_x$ formation and accretion product growth are OH-dependent, and that ozonolysis-driven RO_2 autoxidation independently sustains $C_6H_7O_x$ product formation without OH contribution.

TME addition experiments confirm the contribution of the OH channel, as TME serves as an additional OH source via its reaction with O_3 (Table 2; Fig. 3). At both residence times, TME addition increases $C_6H_9O_x$ signal intensities. Under the elevated OH flux generated by TME ozonolysis, $C_{12}H_{18}O_8$ is additionally detected, forming by direct cross-recombination of $C_6H_9O_4$ and $C_6H_9O_6$ peroxy radicals from the OH channel via intersystem crossing within the $RO\cdots OR'$ complex. Its appearance exclusively under TME conditions reflects the higher RO_2 concentrations required for direct $C_6 + C_6$ recombination to compete with fragmentation pathways.

https://doi.org/10.5194/egusphere-2026-4450
Preprint. Discussion started: 13 August 2026

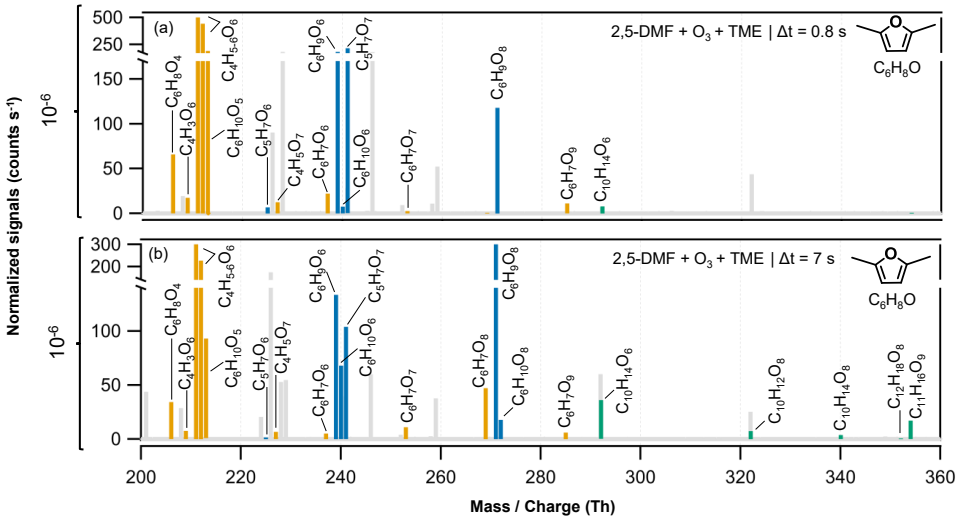

Figure 3. NO_3^- CIMS mass spectra of 2,5-DMF oxidation initiated by OH radicals generated by TME ozonolysis at residence times of (a) 0.8 s: [2,5-DMF] = 1360 ppbv, [O_3] = 117 ppbv, [TME] = 51 ppbv; and (b) 7 s: [2,5-DMF] = 169 ppbv, [O_3] = 54 ppbv, [TME] = 21 ppbv. Peak labels indicate assigned neutral molecular compositions (NO_3^- adduct excluded). O_3-derived monomers ($C_6H_7O_x$) are shown in yellow, OH-derived monomers ($C_6H_9O_x$) in blue, and accretion products in green.

3.2 H/D exchange experiments

H/D exchange with D_2O vapour substitutes labile hydrogen atoms in $-OH$ and $-OOH$ groups with deuterium, producing discrete mass shifts in the NO_3^- CIMS spectra that directly count exchangeable sites per molecule. The $C_6H_7O_x$ series, spanning $C_6H_7O_6$ through $C_6H_7O_9$, shows a uniform $+1$ Da shift (Fig. 4; Table 3), consistent with a single terminal $-OOH$ group and the computed structures (Sect. 3.4.2).

The $C_6H_9O_x$ series displays a different pattern because OH addition to the furan ring adds a hydroxyl group at the initial oxidation step. Subsequent endocyclization and RO_2 autoxidation yield $C_6H_9O_6$ with a $+1$ Da shift and $C_6H_9O_8$ with a $+2$ Da shift, showing that exchangeable hydrogen count increases with oxygenation state. The $+1$ Da shift of $C_6H_9O_6$ is consistent with the computed structure (Sect. 3.4.4). No low-barrier unimolecular pathway to $C_6H_9O_8$ was identified computationally, and its formation pathway remains to be established.

The closed-shell termination products $C_6H_{10}O_6$ and $C_6H_{10}O_8$ exhibit $+2$ and $+3$ mass shifts, respectively. The $+2$ shift of $C_6H_{10}O_6$ is consistent with an $RO_2 + HO_2$ termination product carrying both the hydroxyl group from OH addition and a terminal hydroperoxide. The $+3$ shift of $C_6H_{10}O_8$ reflects an additional labile site introduced by a unimolecular autoxidation step prior to termination.

https://doi.org/10.5194/egusphere-2026-4450
Preprint. Discussion started: 13 August 2026

The $C_5H_7O_7$ fragmentation product retains a single exchangeable hydrogen following β-scission of the C_6 skeleton, shown by a $+1$ Da shift. Accretion products in the C_{10}–C_{12} range show a uniform $+2$ Da shift, consistent with two labile hydrogens from the recombining RO_2 subunits.

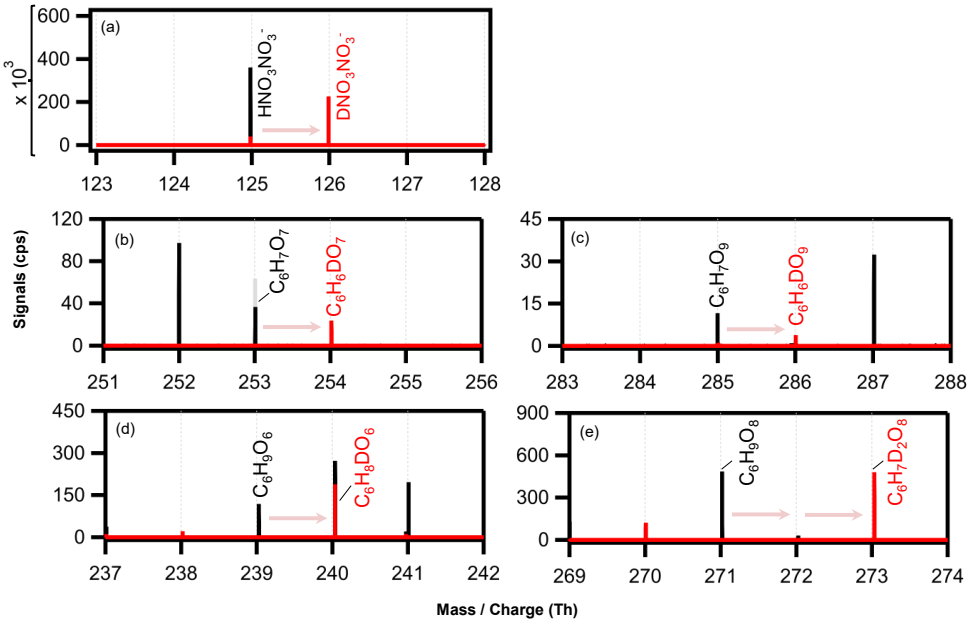

Figure 4. Hydrogen–deuterium exchange experiment during 2,5-DMF ozonolysis at a residence time of 7 s: $[\text{2,5-DMF}] = 254\,\text{ppbv}$ and $[O_3] = 114\,\text{ppbv}$. Spectra show the (a) reagent ion, (b–c) O_3-derived products, and (d–e) OH-derived products with D_2O added to identify labile hydrogen atoms. Peak labels indicate assigned neutral molecular compositions (NO_3^- adduct excluded). Signals from the experiment without D_2O addition are shown in black, while spectra recorded in the presence of D_2O are shown in red. Mass shifts indicate the number of exchangeable (–OH or –OOH) hydrogen atoms.

https://doi.org/10.5194/egusphere-2026-4450
Preprint. Discussion started: 13 August 2026

Table 3. Observed H/D exchange mass shifts (Δm) for monomeric HOMs and accretion products detected during 2,5-DMF ozonolysis and OH-initiated oxidation. Each unit shift corresponds to one labile (–OH or –OOH) hydrogen exchanged by added D_2O.

2,5-DMF + O_3			2,5-DMF + OH		
Type	Formula	Δm (Da)	Type	Formula	Δm (Da)
HOM O_6	$C_6H_7O_6$	+1	Fragment	$C_5H_7O_7$	+1
HOM O_7	$C_6H_7O_7$	+1	HOM O_6	$C_6H_9O_6$	+1
HOM O_8	$C_6H_7O_8$	+1	HOM O_8	$C_6H_9O_8$	+2
HOM O_9	$C_6H_7O_9$	+1	ROOH O_6	$C_6H_{10}O_6$	+2
			ROOH O_8	$C_6H_{10}O_8$	+3
			Accretion	$C_{10}H_{12}O_8$	+2
			Accretion	$C_{10}H_{14}O_6$	+2
			Accretion	$C_{12}H_{18}O_8$	+2
			Accretion	$C_{11}H_{16}O_9$	+2

ROOH = closed-shell $RO_2 + HO_2$ termination product; HOM O_n = highly oxygenated organic molecule with n oxygen atoms; Accretion = bimolecular recombination product; Δm shows the mass unit shift in the presence of D_2O.

3.3 Impact of NO on HOM formation

Addition of 100 ppbv NO at $\Delta t = 7$ s suppresses autoxidation and redirects RO_2 radicals toward organonitrate ($RONO_2$) formation (Fig. 5). The nitrogen-containing series $C_6H_9O_{4–9}NO$ dominates the spectrum, with $C_6H_9O_5NO$, $C_6H_9O_6NO$, and $C_6H_9O_4NO$ as the three highest-intensity products. The lower-oxygen members $C_6H_9O_{4–6}NO$ form by direct $RO_2 + NO$ termination of OH-initiated peroxy radicals at successive autoxidation stages. The higher-oxygen members $C_6H_9O_7NO$ and $C_6H_9O_9NO$ form via an alkoxy radical intermediate: $RO_2 + NO$ first produces RO, which undergoes H-shift and O_2 addition to regenerate a more oxygenated RO_2, and a second $RO_2 + NO$ reaction then yields the observed organonitrate. An ozonolysis-derived organonitrate, $C_6H_7O_7NO$, is also detected, confirming that $RO_2 + NO$ termination competes with autoxidation in both radical channels.

At 100 ppbv NO, all HOM monomers, closed-shell termination products, and accretion products fall below the detection limit. The near-complete redistribution of signal to organonitrates confirms that the HOM and accretion products observed in NO-free experiments originate from peroxy radical chemistry, and that NO at this mixing ratio suppresses both unimolecular autoxidation and bimolecular $RO_2 + RO_2$ recombination.

https://doi.org/10.5194/egusphere-2026-4450
Preprint. Discussion started: 13 August 2026

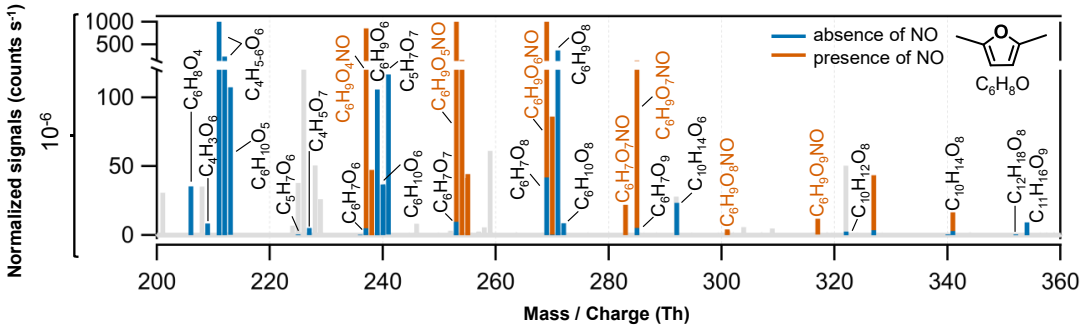

Figure 5. NO_3^- CIMS mass spectra of 2,5-DMF ozonolysis at $\Delta t = 7$ s in the absence (blue) and presence (orange) of NO. Experimental conditions: [2,5-DMF] = 169 ppbv, $[O_3] = 54$ ppbv, and [NO] = 100 ppbv. Peak labels indicate assigned neutral molecular compositions (NO_3^- adduct excluded).

3.4 Mechanistic Discussion

3.4.1 Formation of Criegee Intermediates and Conformer Description

The formation of the primary ozonide from the ozonolysis of 2,5-DMF, followed by its decomposition into the Criegee intermediates CI-1 and CI-2, is shown in Fig. 6. These Criegee intermediates can be classified as Syn and Anti, based on the orientation of the terminal –OO group relative to the nearby substituent (Watson et al., 2025; Kao et al., 2024; Vereecken et al., 2015). These conformers can coexist under identical conditions and exhibit distinct unimolecular reactivity, with rate coefficients differing by several orders of magnitude (Campos-Pineda et al., 2025; Hakala and Donahue, 2023; Huang et al., 2025; Lin et al., 2015; Long et al., 2016; Luo et al., 2025; Sheps et al., 2014; Taatjes et al., 2013). In this work, the Syn and Anti conformers of CI-1 differ in the orientation of the terminal –OO group relative to the adjacent methyl group, whereas in CI-2, the distinction is defined by its orientation relative to the vicinal hydrogen on the carbonyl oxide carbon. Substitution, steric constraints, and functional group environment can influence which pathways are accessible, including hydrogen shifts, dioxirane formation, or intramolecular cyclization (Lakmuang et al., 2020; Long et al., 2019; Vereecken et al., 2022; Yin and Takahashi, 2017).

https://doi.org/10.5194/egusphere-2026-4450
Preprint. Discussion started: 13 August 2026

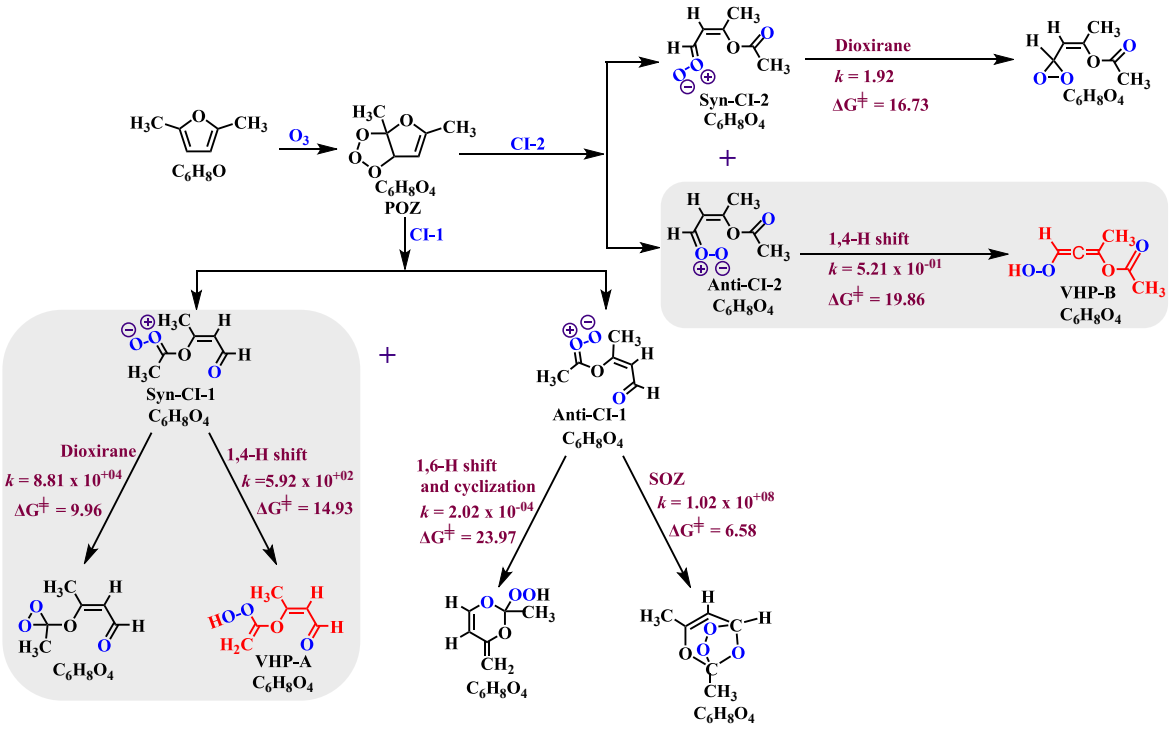

Figure 6. Ozonolysis of 2,5-DMF showing the formation of a POZ, followed by its decomposition into CI-1 and CI-2, with Syn conformers (highlighted in grey-shaded boxes) and their corresponding Anti conformers. The subsequent unimolecular reaction pathways for Syn-CI-1 are dioxirane formation and 1,4-H shift; for Anti-CI-1 are SOZ formation and concerted 1,6-H shift with cyclization; for Syn-CI-2 is dioxirane formation; and for Anti-CI-2 is 1,4-H shift. Rate coefficients (k, s^{-1}) and barrier heights ($\Delta G^{\ddagger}$, kcal mol^{-1}) were calculated at the RHF-RCCSD(T)-F12a/VDZ-F12//M06-2X/aug-cc-pVTZ level of theory. Colour code: red highlights key intermediates, while blue oxygen atoms indicate those originating from O_3.

In the present study, IRC calculations following POZ decomposition connected the product geometries to the Syn conformers of both CI-1 and CI-2. The corresponding POZ conformer lies 3.61 kcal mol^{-1} above the global-minimum POZ structure. Syn-CI-1 lies ∼13 kcal mol^{-1} higher in energy than Syn-CI-2 and is formed via a higher decomposition barrier (22.6 kcal mol^{-1}) than Syn-CI-2 (17.7 kcal mol^{-1}), as illustrated by the potential energy surface in Fig. 7. The branching fractions for chemically activated POZ decomposition leading to Syn-CI-1 and Syn-CI-2 were calculated using MESMER and found to be 5.52% and 94.48%, respectively.

https://doi.org/10.5194/egusphere-2026-4450
Preprint. Discussion started: 13 August 2026

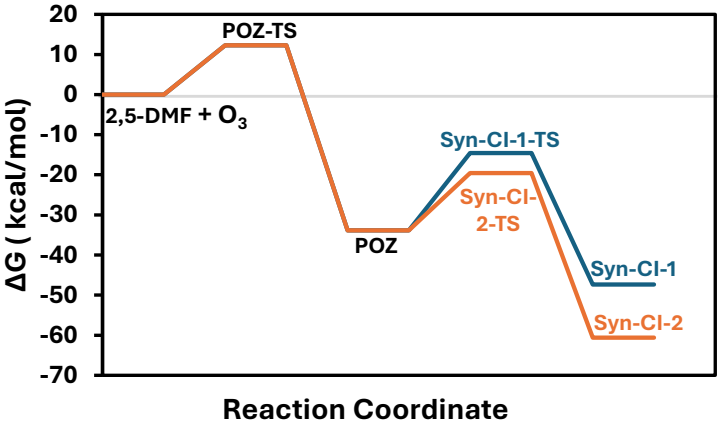

Figure 7. Gibbs free energy profile for the decomposition of the POZ formed during the ozonolysis of 2,5-DMF leading to the Syn conformers of CI-1 and CI-2. Gibbs free energies (ΔG, kcal mol^{-1}) are shown along the y-axis and the reaction coordinate along the x-axis. TS = transition state, POZ = primary ozonide, and CI = Criegee intermediate.

As illustrated in Fig. 6, for the 2,5-DMF system, the Syn-CI-1 conformer is favourably oriented for a 1,4-hydrogen shift leading to VHP-A formation. However, the calculated rate coefficients indicate that dioxirane formation constitutes the dominant pathway for this conformer. Based on previous experimental evidence for the coexistence of Syn and Anti conformers, we also examined the reactivity of the Anti-CI-1 conformer, which preferentially undergoes intramolecular cyclization to form a secondary ozonide (SOZ), strongly dominating over the 1,6-hydrogen shift leading to the cyclic structure. Although dioxirane formation is often associated with Anti-CI conformers in previous studies (Drozd et al., 2017; Kroll et al., 2002), no transition state for dioxirane formation could be located for the Anti-CI-1 conformer in the present system. Instead, a dioxirane pathway was identified for the Syn conformer. This behaviour likely reflects conformer-specific geometric constraints that disfavour the three-membered ring closure required for dioxirane formation.

CI-2 likewise exhibits pronounced conformer-specific reactivity. The only viable pathway identified for Syn-CI-2 is dioxirane formation, whereas a 1,4-hydrogen-shift pathway leading to VHP-B was identified for Anti-CI-2. Although vinylic hydrogen abstraction typically involves high barriers ($\sim$25 kcal mol^{-1}), the barrier here is lower ($\sim$19.86 kcal mol^{-1}), likely due to conjugation with the adjacent peroxide functionality, resulting in pseudo-allylic character and facilitating the hydrogen shift (Guo et al., 2023; Vereecken and Nozière, 2020).

3.4.2 Criegee intermediate chemistry leading to HOM formation

Along the VHP-A pathway, this intermediate undergoes OH elimination to form a carbon-centered radical ($C_6H_7O_3$), which subsequently reacts with O_2 to form a peroxy radical intermediate ($C_6H_7O_5$), as shown in Fig. **??**.

https://doi.org/10.5194/egusphere-2026-4450
Preprint. Discussion started: 13 August 2026

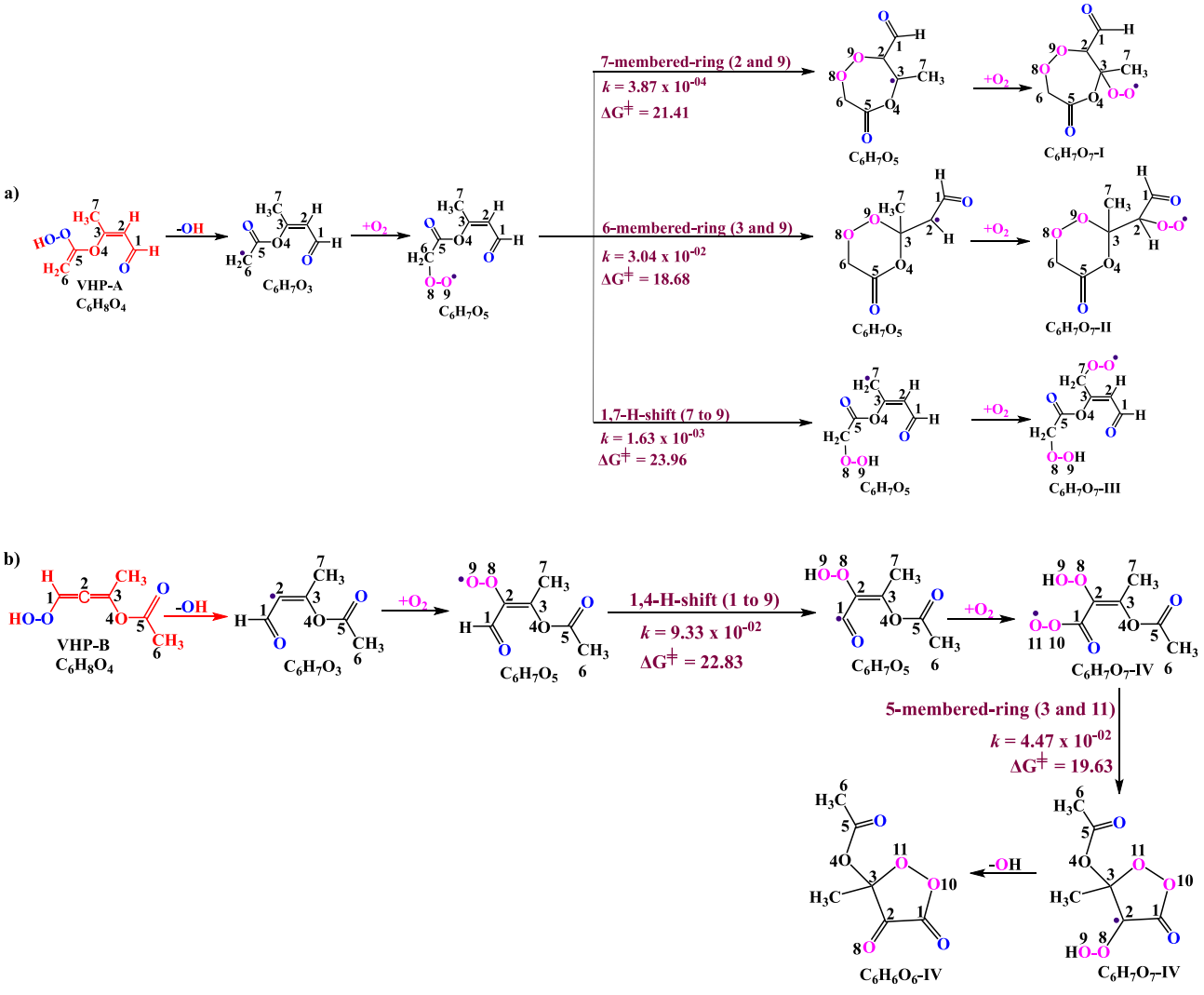

Figure 8. Reaction pathways for the formation of HOMs up to O_7 species initiated by (a) VHP-A produced from Syn-CI-1 and (b) VHP-B produced from Anti-CI-2, showing the key intermediates and product-forming steps. Rate coefficients (k, s^{-1}) and barrier heights ($\Delta G^{\ddagger}$, kcal mol^{-1}) were calculated at the ROHF-RCCSD(T)-F12a/VDZ-F12//M06-2X/aug-cc-pVTZ level of theory. Colour code: The red structure denotes the starting intermediate from which all pathways originate. Blue oxygen atoms indicate those originating from O_3, while pink oxygen atoms represent O_2 addition.

315 The resulting $C_6H_7O_5$ can undergo several competing unimolecular pathways which include intramolecular ring-closure reactions leading to six- and seven-membered cyclic products, as well as a 1,7-hydrogen-shift pathway, with calculated branching ratios of 93.77%, 1.19%, and 5.04%, respectively (based on the rate coefficients calculated using the MC-TST method). A 1,8-hydrogen-shift pathway was also explored, but no transition state could be located. Although all considered pathways yield O_7

https://doi.org/10.5194/egusphere-2026-4450
Preprint. Discussion started: 13 August 2026

products ($C_6H_7O_7$-I, II and III), the resulting molecular structures differ. The six- and seven-membered ring-closure pathways produce O_7 species that are unlikely to be detected by NO_3^--CIMS due to the absence of –OH or –OOH functional groups required for binding with NO_3^-. In contrast, the 1,7-hydrogen-shift pathway gives an O_7 product containing a –OOH group which is likely detectable by NO_3^--CIMS. Calculated barrier heights further showed that Syn-CI-1-derived autoxidation does not proceed beyond O_7, as all subsequent oxidation steps involve barriers exceeding 25 kcal mol^{-1} (Section S4, Fig S4a). Consistent with the D_2O experiments (Fig. 4), the observed +1 mass shift indicates that O_7 formed via the 1,7-hydrogen-shift channel contains one exchangeable hydrogen atom that undergoes H/D exchange, supporting the proposed hydroperoxide functionality and the mechanistically derived structure.

The pathways explored for Anti-CI-1 and Syn-CI-2 predominantly lead to closed-shell products (Fig. 6). For Anti-CI-2, however, the only viable pathway identified is a 1,4-hydrogen shift forming VHP-B ($k = 5.21 \times 10^{-1}$ s^{-1}, $\Delta G^{\ddagger} = 19.86$ kcal mol^{-1}; Fig. 6), which may contribute to O_7 species ($C_6H_7O_7$-IV) and may subsequently form the closed-shell product $C_6H_6O_6$, as shown in Fig. 8b. No additional pathways of comparable atmospheric relevance were identified, as alternative channels involved higher barriers (>25 kcal mol^{-1}; see Section S4, Fig S4b).

While HOM monomers containing up to O_9 were observed within the experimental residence time of 0.8 s, the pathways explored for Syn-CI-1 and Anti-CI-2 were not found to efficiently progress beyond O_7 under atmospheric conditions within the present computational framework. This motivated the exploration of additional pathways that could contribute to rapid O_9 formation. Accordingly, alongside the 1,4-hydrogen shift pathway for Anti-CI-2 (Fig. 6), a 1,6-hydrogen shift was also explored. However, no transition state could be located from the conventional Anti-CI-2 geometry, indicating that this pathway is not readily accessible (Vereecken and Nozière, 2020). Instead, IRC analysis of the located 1,6-hydrogen shift transition state showed that it is associated with a distinct CI-2-like structure, denoted here as Anti-CI-2A (Fig. 9), in which the hydrogen and methyl groups are positioned on opposite sides of the conjugated π system, with the –OO group oriented away from the vicinal hydrogen.

https://doi.org/10.5194/egusphere-2026-4450
Preprint. Discussion started: 13 August 2026

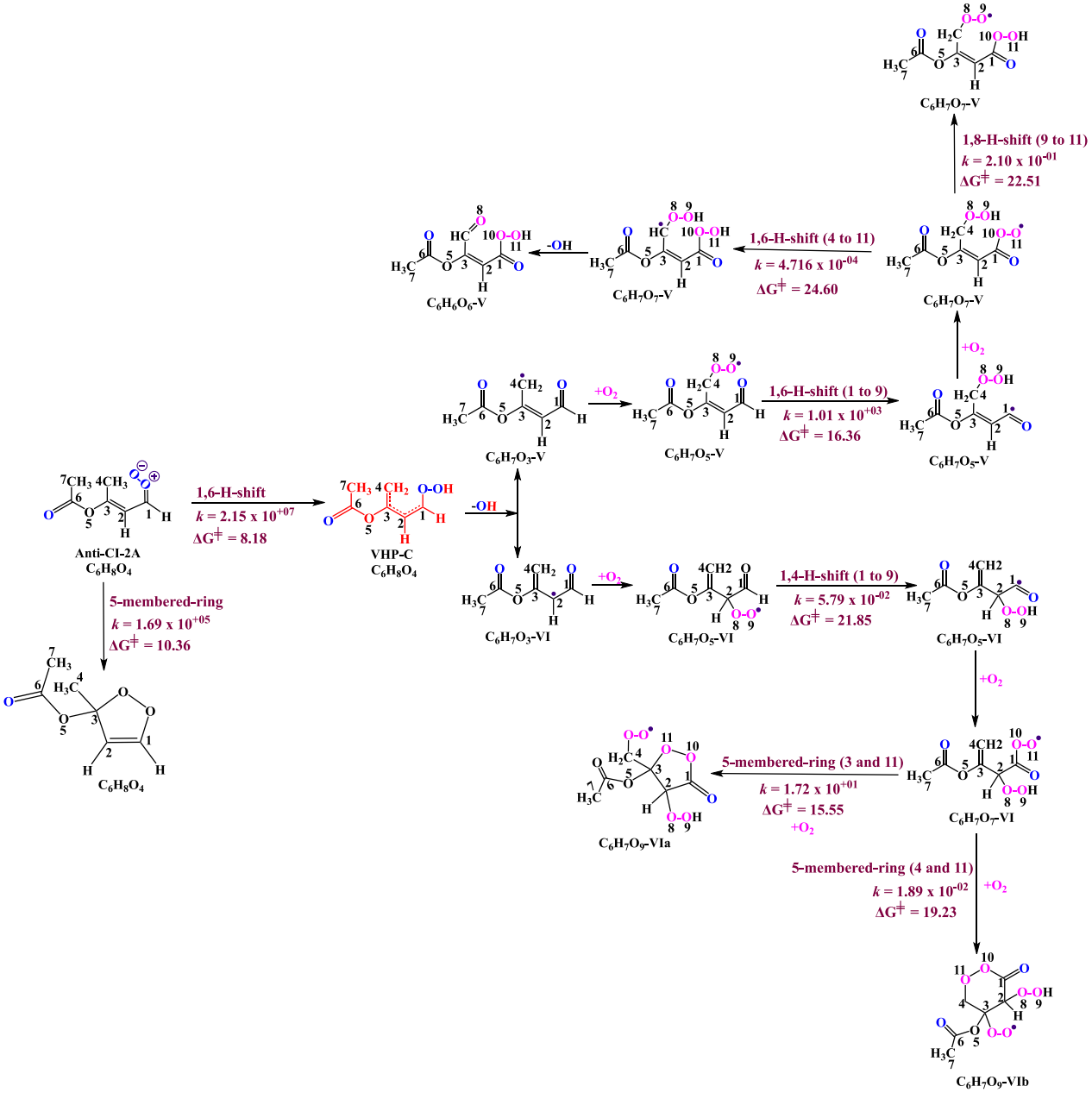

Figure 9. Reaction pathway for the formation of HOMs up to O_9 species initiated by the Anti-CI-2A geometry, showing the key intermediates and product-forming steps. Rate coefficients (k, s^{-1}) and barrier heights ($\Delta G^{\ddagger}$, kcal mol^{-1}) were calculated at the ROHF-RCCSD(T)-F12a/VDZ-F12//M06-2X/aug-cc-pVTZ level of theory. Colour code: The red structure denotes the intermediate VHP-C from which all pathways originate. Blue oxygen atoms indicate those originating from O_3, while pink oxygen atoms represent O_2 addition.

https://doi.org/10.5194/egusphere-2026-4450
Preprint. Discussion started: 13 August 2026

Vereecken et al. have reported that allylic 1,6-hydrogen-shift reactions in oxygenated and unsaturated Criegee intermediates can be fast ($\approx 10^6$–10^8 s^{-1}) when enabled by appropriate molecular geometry (Vereecken et al., 2022). In line with this behaviour, Anti-CI-2A exhibits a 1,6-hydrogen-shift pathway leading to VHP-C and a competing five-membered ring-closure pathway forming a closed-shell product. Using the lowest-energy Anti-CI-2A conformer obtained from conformational sampling as the reactant reference yields rate coefficients of $k \approx 2.15 \times 10^7$ s^{-1} ($\Delta G^{\ddagger} = 8.18$ kcal mol^{-1}) for the 1,6-hydrogen shift and $k \approx 1.69 \times 10^5$ s^{-1} ($\Delta G^{\ddagger} = 10.36$ kcal mol^{-1}) for the five-membered ring closure. Referencing the barriers to the IRC-connected reactant conformer instead gives rate coefficients of approximately 10^{10} and 10^7 s^{-1}, respectively. Despite this conformer dependence, both treatments indicate that the 1,6-hydrogen-shift pathway remains highly competitive on the experimental timescale, and the qualitative conclusion regarding the kinetic feasibility of VHP-C formation remains unchanged.

Further exploration of the subsequent autoxidation chemistry indicated that this pathway can mechanistically explain the formation of O_9 species. As illustrated in Fig. 9, formation of VHP-C followed by OH elimination yields a carbon-centered radical ($C_6H_7O_3$-V) and its alternative resonance form ($C_6H_7O_3$-VI). Subsequent O_2 addition to $C_6H_7O_3$-V forms a peroxy radical ($C_6H_7O_5$-V), from which several unimolecular pathways were examined. Among these, the 1,6-hydrogen shift was found to be kinetically favored with $k = 1.01 \times 10^3$ s^{-1} and $\Delta G^{\ddagger} = 16.36$ kcal mol^{-1}, while all other channels exhibited barriers exceeding 30 kcal mol^{-1} (see Section S4, Fig S4). Further O_2 addition leads to $C_6H_7O_7$-V. Although additional autoxidation steps could, in principle, form $C_6H_7O_9$-V via pathways such as a 1,6-hydrogen shift and hydrogen-scrambling, these routes are likely not competitive. The 1,6-hydrogen shift is too slow and is followed by rapid OH loss, yielding $C_6H_6O_6$-V. Further downstream channels of the hydrogen-scrambling route were investigated, they are also unlikely to contribute to O_9 formation (see Section S4, Fig S5).

Whereas $C_6H_7O_3$-VI undergoes rapid O_2 addition, after which the subsequent 1,4-hydrogen shift constitutes the primary kinetic bottleneck and governs the formation of $C_6H_7O_7$-VI. Subsequent ring-closure reactions yield five- and six-membered cyclic products and proceed with branching ratios of approximately 98% and 2%, respectively, followed by O_2 addition leading to $C_6H_7O_9$-VIa and $C_6H_7O_9$-VIb. Consistent with this mechanism, D_2O-labeling experiments (Fig. 4) showed a +1-mass shift for both O_7 and O_9 species, indicating the presence of one exchangeable hydrogen atom associated with a –OOH functionality. Kinetically, autoxidation initiated from $C_6H_7O_3$-V favors rapid accumulation of O_7, whereas the pathway via $C_6H_7O_3$-VI provides a viable route toward O_9 formation.

Although Anti-CI-2A was found to account for HOM formation up to O_9 on the experimental timescale within the present computational framework, its formation pathway could not be established, as the IRC calculations employed in the present study connected POZ decomposition only to the conventional Syn-CI-1 and Syn-CI-2 geometries. Therefore, one possible route involving internal rotation of the methyl/hydrogen orientation in the conventional CI-2 geometry was explored. The interconversion was found to involve a high rotational barrier of approximately 56 kcal mol^{-1} at the UM06-2X/aug-cc-pVTZ level of theory (Guess=Mix, Always), suggesting difficult conformational interconversion under atmospheric conditions, although the exact magnitude may be method-dependent. This restricted rotation is likely due to conjugation between the >C=OO moiety and the adjacent C=C bond, which imparts partial double-bond character to the connecting C–C bond. Another possibility is that, by analogy with the Syn and Anti Criegee intermediates formed directly during primary ozonide decomposition,

https://doi.org/10.5194/egusphere-2026-4450
Preprint. Discussion started: 13 August 2026

Anti-CI-2A may also be populated during the chemically activated decomposition of the primary ozonide (Peltola et al., 2024; Vereecken et al., 2015).

3.4.3 Kinetic modelling for CI pathways to O_9 HOMs

To evaluate the potential role of Anti-CI-2A, sensitivity tests were performed using Kinetiscope. First, the POZ concentration (molecules cm^{-3}) was obtained after simulating the reaction scheme for 7 s, mimicking the experimental conditions (1360 ppbv 2,5-DMF and 117 ppbv O_3, corresponding to the short residence-time experiment of 0.8 s). All rate coefficients used in the simulations were obtained from calculations performed in this study using transition state theory, with additional values taken from the literature where necessary, as described in detail in Section S5 of the Supplementary Information. POZ decomposition into Syn-CI-1 and Syn-CI-2 was then simulated to determine the corresponding CI populations. At the 1×10^8 total particle number setting, the average species distribution over the 7 s simulation period consisted of approximately 99.93% Syn-CI-2, 0.025% Syn-CI-1, with the remaining 0.046% present as unreacted POZ. To account for the excess energy retained in the chemically activated POZ decomposition, the POZ decomposition rate coefficients were additionally adjusted to reproduce the MESMER branching ratio (≈5.5% Syn-CI-1 and ≈94.5% Syn-CI-2). The average CI concentrations obtained using both the TST and MESMER-adjusted rate coefficients were then used as the initial species concentrations in a simplified kinetic scheme initiated directly from the Criegee intermediates and following the reaction pathways identified in this study toward highly oxygenated products (O_7–O_9). Equal populations of the corresponding Anti conformers were assumed because conformer-specific formation rate coefficients were unavailable. To evaluate the influence of Anti-CI-2A on the computed reaction pathways from Syn- and Anti-CI, this conformer was additionally introduced at 0.01% of the average POZ population obtained from the 7 s simulations to explore its potential role in O_9 formation.

The simulations showed that the O_9 product, $C_6H_7O_9$-VIa (Fig. **??**), forms on a sub-second timescale. While the onset time exhibited some stochastic variability (0.002–0.064 s) across different random number seeds, the predicted average concentration of $C_6H_7O_9$-VIa remained consistently on the order of 10^5 molecules cm^{-3} (Table S3). These results suggest that even a minor contribution (0.01% of the average POZ population) from a highly reactive CI-2-like geometry such as Anti-CI-2A may be sufficient to account for the observed O_9 formation. While the formation pathway of Anti-CI-2A could not be directly established, the results indicate that access to such a reactive geometry provides a plausible kinetic route to HOM formation on the experimental timescale.

3.4.4 OH-initiated pathways to HOM formation

Rate coefficients for OH reactions with furan and alkylated furans have been reported previously, consistently showing that OH addition dominates over hydrogen abstraction under atmospheric conditions (Elwardany et al., 2016; Whelan et al., 2020; Yuan et al., 2017). In the present work, the calculated rate coefficient for the reaction of OH with 2,5-DMF is in close agreement with earlier studies, with a value of k(OH + 2,5-DMF) = $(12.5 \pm 0.4) \times 10^{-11}$ cm^3 $molecule^{-1}$ s^{-1} (Aschmann et al., 2011; Bierbach et al., 1992), as shown in Fig. 10. The reaction is dominated by OH addition at the 2-position of the furan ring, accounting

https://doi.org/10.5194/egusphere-2026-4450
Preprint. Discussion started: 13 August 2026

for approximately 98.18% of the total reactivity due to favourable electronic stabilization. Minor contributions arise from OH addition at the 3-position and from hydrogen abstraction from the methyl group.

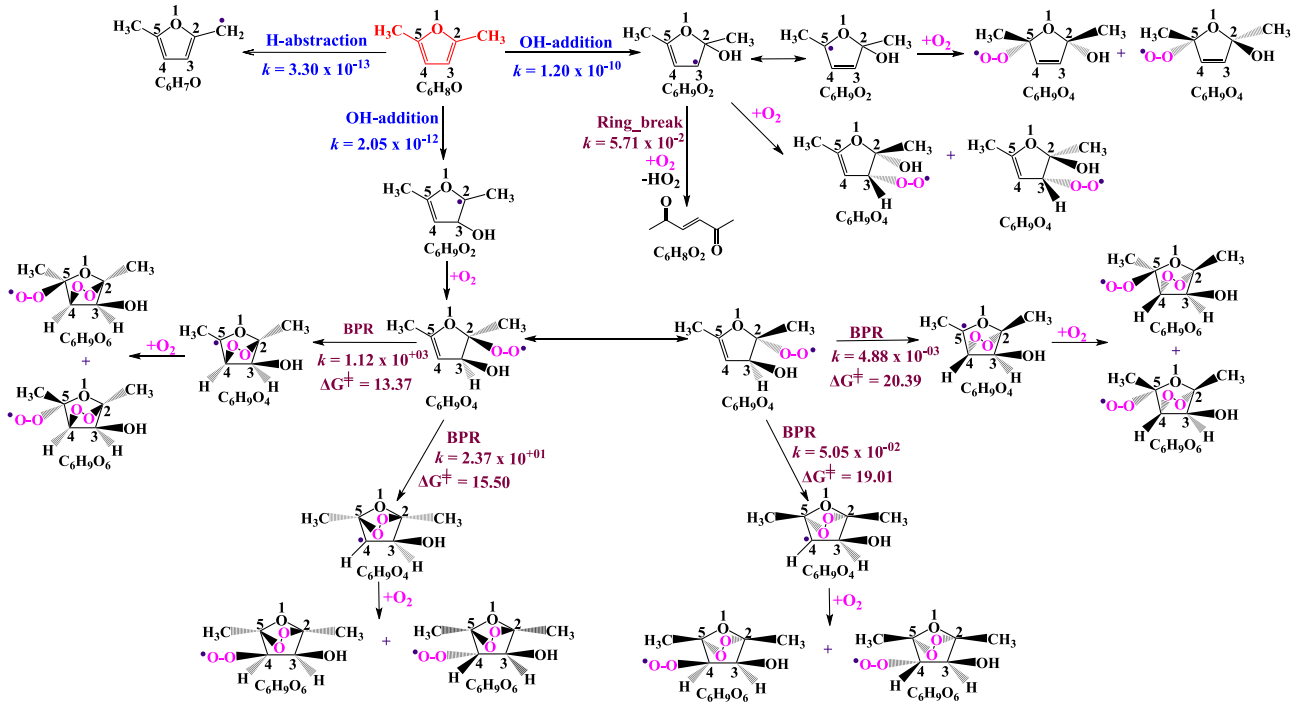

Figure 10. Reaction pathways for the formation of HOMs up to O_6 species initiated by OH addition to 2,5-DMF (red), highlighting key intermediates and product-forming steps. Bimolecular reaction rate coefficients (k, cm^3 molecule^{-1} s^{-1}) are shown in blue, while unimolecular reaction rate coefficients (k, s^{-1}) and barrier heights ($\Delta G^{\ddagger}$, kcal mol^{-1}) are shown in purple. O_2 addition is indicated by pink oxygen atoms. All rate coefficients were calculated at the ROHF-RCCSD(T)-F12a/VDZ-F12//M06-2X/aug-cc-pVTZ level of theory.

After the addition of OH at the 2nd position, the hydroxy-substituted carbon-centered radical formed can either undergo unimolecular ring opening to form ring-cleaved closed-shell products on a slow timescale ($\sim 10^{-2}$ s^{-1}) or react rapidly with O_2 with a pseudo-unimolecular rate coefficient of $\sim 10^7$ s^{-1}. Consequently, the latter is expected to dominate and lead to efficient formation of $C_6H_9O_4$. Further, all explored intramolecular H-shift and cyclization pathways through this channel exhibited barriers >29 kcal mol^{-1}, favouring bimolecular over unimolecular processes (Section S4, Figs S6).

In contrast, the minor OH-addition channel at the 3rd position (branching ratio = 1.56%) enabled ring closure and bicyclic peroxy radical (BPR) formation. As illustrated in Fig. 10, ring closure leading to BPR formation is strongly favored when the –OH and –OO groups reside on the same side, consistent with stabilization by intramolecular OH—OO interaction, whereas opposite-side orientations resulted in relatively slower cyclization. Subsequent O_2 addition led to HOM formation containing O_6 species, which is structurally supported by D_2O labelling experiments showing a +1-mass shift, as expected due to the

https://doi.org/10.5194/egusphere-2026-4450
Preprint. Discussion started: 13 August 2026

presence of one –OH group. For unimolecular oxidation pathways beyond O_6, we could not identify viable routes that can explain the formation of O_8; all pathways located exhibit high barriers and are reported in Section S4 (Figs S7, S8, and S9).

4 Atmospheric implications

2,5-DMF is emitted in biomass burning and from biofuel combustion (Koss et al., 2018; Andreae, 2019) and is efficiently removed by reactions with O_3, OH, and NO_3 in the troposphere, with atmospheric lifetimes on the order of hours under background oxidant concentrations. Both oxidation pathways produce HOM spanning O:C = 1.00–1.50. These low-volatility products are not detectable by conventional techniques such as FTIR and PTR-ToF-MS and may contribute to the $>50\,\%$ carbon balance deficit reported by Illmann and Rösgen (2024). The absence of homogeneous nucleation in prior chamber studies (Tajuelo et al., 2021) indicates a condensation-limited outcome, where the products formed require pre-existing aerosol surfaces for efficient partitioning.

Under elevated NO_x, RO_2 radicals are rapidly intercepted by $RO_2 + NO$ reactions, suppressing autoxidation and shifting the product distribution toward organonitrates, which reduces HOM formation. Under low NO_x conditions, longer RO_2 lifetimes allow autoxidation to proceed, shifting the product distribution toward higher-oxygen, lower-volatility monomers. Such conditions are more representative of aged biomass burning plumes, where the contribution of 2,5-DMF oxidation to SOA formation via condensation onto pre-existing aerosol is expected to be enhanced.

5 Conclusions

The gas-phase oxidation of 2,5-DMF by O_3 and OH was investigated using flow reactor experiments and quantum chemical calculations to characterize HOM formation and elucidate the underlying reaction mechanisms. While previous studies established the primary oxidation products and reaction pathways of 2,5-DMF (Illmann and Rösgen, 2024), the present study characterizes the subsequent autoxidation chemistry leading to the rapid formation of HOM through both ozonolysis and OH-initiated oxidation. Both ozonolysis and OH-initiated oxidation produced HOM monomers within $\Delta t = 0.8$ s, confirming that intramolecular H-shift-mediated autoxidation proceeds efficiently in this system. Ozonolysis formed HOM species containing up to nine oxygen atoms (O_9), whereas OH-initiated oxidation formed HOM species containing up to eight oxygen atoms (O_8). At $\Delta t = 7$ s, elevated RO_2 concentrations promoted bimolecular pathways, producing closed-shell RO_2 + HO_2 termination products and accretion products. NO addition suppressed these autoxidation pathways and redirected product distributions toward organonitrate formation, demonstrating that RO_2 + NO reactions dominate under high-NO_x conditions. Together, these results show that the oxidation chemistry evolves from rapid unimolecular autoxidation on sub-second timescales to bimolecular RO_2 chemistry as the reaction progresses, extending the unimolecular RO_2 isomerization behaviour previously reported for the DICARBO2 radical (Illmann and Rösgen, 2024) to a broader network of autoxidation pathways accessible in this system.

Complementary quantum chemical calculations provided a mechanistic framework for interpreting the experimental observations by identifying the dominant reaction pathways and evaluating the reactivity of the corresponding Criegee intermediate

https://doi.org/10.5194/egusphere-2026-4450
Preprint. Discussion started: 13 August 2026

geometries. In the present study, a distinct CI geometry termed Anti-CI-2A was identified as a plausible route to HOM species containing up to nine oxygen atoms (O_9) on the experimental timescale of 0.8 s, owing to a rapid 1,6-H shift ($k \approx 10^7$ s^{-1}). However, the formation pathway of this particular Criegee intermediate could not be directly established using the quantum chemical approaches employed here. Kinetic simulations nevertheless suggested that even a minor population of Anti-CI-2A may be sufficient to influence subsequent reaction pathways leading to HOM formation. These findings suggest that POZ decomposition in structurally complex ozonolysis systems may access additional reactive CI geometries beyond the conventional Syn/Anti conformers. For the OH-initiated oxidation pathway, the calculations provided a mechanistic explanation for HOM formation up to O_6, whereas the pathways leading to the experimentally observed O_8 HOM monomers could not be established within the explored reaction mechanisms. Together, the experimental observations and mechanistic calculations provide new insight into the rapid formation of HOM from 2,5-DMF and establish a mechanistic framework that may also aid the interpretation of the atmospheric oxidation chemistry of related methylated furan derivatives. The rapid formation of low-volatility HOM observed here further indicates that autoxidation of 2,5-DMF and related biomass-burning-derived furans can provide condensable vapours that may contribute to SOA growth in biomass-burning plumes.

Data availability. Details of the experimental setup, mass spectrometry instrumentation, chemicals and gas cylinder specifications, kinetic modelling reaction schemes, and additional reaction channels explored in this study are provided in the Supplementary Information. All corresponding computational files (.log and .out) together with the MESMER input file (.xml) are available in the Zenodo repository: https://doi.org/10.5281/zenodo.21300445

Author contributions. Conceptualization: MR, RA, SJ, SB, AK; data curation: RA, AK, SB, SF; formal analysis: RA, AK, SB; investigation: RA, SJ, AK, SB, PS, SF, SI, MR; methodology: RA, AK, SB, MR; writing (original draft preparation): RA, SJ; writing (review and editing): RA, SJ, AK, SI, MR; funding acquisition: SI, MR.

Competing interests. The authors declare that they have no conflict of interest.

Acknowledgements. We thank the Orbitools team for providing the data analysis program. CSC IT Center for Science in Espoo, Finland, is acknowledged for providing the computing resources.

Financial support. This research has been supported by the H2020 European Research Council (grant no. 101002728), the HORIZON EUROPE European Research Council (grant no. 101096133), the Research Council of Finland (grant nos. 331207, 336531, 346373, 353836, and 355966)

https://doi.org/10.5194/egusphere-2026-4450
Preprint. Discussion started: 13 August 2026

References

Andreae, M. O.: Emission of trace gases and aerosols from biomass burning – an updated assessment, Atmos. Chem. Phys., 19, 8523–8546, https://doi.org/10.5194/acp-19-8523-2019, 2019.

Aschmann, S. M., Nishino, N., Arey, J., and Atkinson, R.: Kinetics of the reactions of OH radicals with 2- and 3-methylfuran, 2,3- and 2,5-dimethylfuran, and E- and Z-3-hexene-2,5-dione, and products of OH + 2,5-dimethylfuran, Environ. Sci. Technol., 45, 1859–1865, https://doi.org/10.1021/es103207k, 2011.

Atkinson, R. and Arey, J.: Atmospheric degradation of volatile organic compounds, Chem. Rev., 103, 4605–4638, https://doi.org/10.1021/cr0206420, 2003.

Atkinson, R. and Carter, W. P. L.: Kinetics and mechanisms of the gas-phase reactions of ozone with organic compounds under atmospheric conditions, Chem. Rev., 84, 437–470, https://doi.org/10.1021/cr00063a002, 1984.

Atkinson, R., Aschmann, S. M., and Carter, W. P. L.: Kinetics of the reactions of O_3 and OH radicals with furan and thiophene at 298 $\pm$ 2 K, Int. J. Chem. Kinet., 15, 51–61, https://doi.org/10.1002/kin.550150106, 1983.

Bierbach, A., Barnes, I., and Becker, K. H.: Rate coefficients for the gas-phase reactions of hydroxyl radicals with furan, 2-methylfuran, 2-ethylfuran and 2,5-dimethylfuran at 300 $\pm$ 2 K, Atmos. Environ., 26, 813–817, https://doi.org/10.1016/0960-1686(92)90241-C, 1992.

Bruce, F. N. O. and Li, Y.: Probing the thermochemistry properties and rate kinetics of trimethyl phosphate (TMP): an H-atom abstraction (HAA) reactions perspective, ACS Omega, 8, 47 134–47 145, https://doi.org/10.1021/acsomega.3c07137, 2023.

Cabañas, B., Baeza, M. T., Salgado, S., Martín, P., Taccone, R., and Martínez, E.: Oxidation of heterocycles in the atmosphere: kinetic study of their reactions with NO_3 radical, J. Phys. Chem. A, 108, 10 818–10 823, https://doi.org/10.1021/jp046524t, 2004.

Campos-Pineda, M., Yang, L., and Zhang, J.: Direct measurement of the Criegee intermediate CH_2OO in ozonolysis of ethene, Nat. Commun., 16, 6515, https://doi.org/10.1038/s41467-025-61739-5, 2025.

Castañeda, R., Iuga, C., Álvarez-Idaboy, J. R., and Vivier-Bunge, A.: Rate constants and branching ratios in the oxidation of aliphatic aldehydes by OH radicals under atmospheric conditions, J. Mex. Chem. Soc., 56, ???–???, https://doi.org/10.29356/jmcs.v56i3.296, 2012.

Crounse, J. D., Nielsen, L. B., Jørgensen, S., Kjaergaard, H. G., and Wennberg, P. O.: Autoxidation of organic compounds in the atmosphere, J. Phys. Chem. Lett., 4, 3513–3520, https://doi.org/10.1021/jz4019207, 2013.

Drozd, G. T., Kurtén, T., Donahue, N. M., and Lester, M. I.: Unimolecular Decay of the Dimethyl-Substituted Criegee Intermediate in Alkene Ozonolysis: Decay Time Scales and the Importance of Tunneling, J. Phys. Chem. A, 121, 6036–6045, https://doi.org/10.1021/acs.jpca.7b05495, 2017.

Durán, R., Barrales-Martínez, C., Solorza, J., and Alzate-Morales, J.: Computational Study of the 1,3-Dipolar Cycloaddition between Criegee Intermediates and Linalool: Atmospheric Implications, J. Phys. Chem. A, 129, 1099–1115, https://doi.org/10.1021/acs.jpca.4c06728, 2025.

Ehn, M., Thornton, J. A., Kleist, E., Sipilä, M., Junninen, H., Pullinen, I., Springer, M., Rubach, F., Tillmann, R., Lee, B., Lopez-Hilfiker, F., Andres, S., Acir, I.-H., Rissanen, M., Jokinen, T., Schobesberger, S., Kangasluoma, J., Kontkanen, J., Nieminen, T., Kurten, T., Nielsen, L. B., Jørgensen, S., Kjaergaard, H. G., Canagaratna, M., Maso, M. D., Berndt, T., Petäjä, T., Wahner, A., Kerminen, V.-M., Kulmala, M., Worsnop, D. R., Wildt, J., and Mentel, T. F.: A large source of low-volatility secondary organic aerosol, Nature, 506, 476–479, https://doi.org/10.1038/nature13032, 2014.

https://doi.org/10.5194/egusphere-2026-4450
Preprint. Discussion started: 13 August 2026

Elwardany, A., Es-sebbar, E., Khaled, F., and Farooq, A.: A chemical kinetic study of the reaction of hydroxyl with furans, Fuel, 166, 245–252, https://doi.org/10.1016/j.fuel.2015.10.098, 2016.

Frisch, M. J., Trucks, G. W., Schlegel, H. B., Scuseria, G. E., Robb, M. A., Cheeseman, J. R., Scalmani, G., Barone, V., Petersson, G. A., Nakatsuji, H., Li, X., Caricato, M., Marenich, A. V., Bloino, J., Janesko, B. G., Gomperts, R., Mennucci, B., Hratchian, H. P., Ortiz, J. V., Izmaylov, A. F., Sonnenberg, J. L., Williams-Young, D., Ding, F., Lipparini, F., Egidi, F., Goings, J., Peng, B., Petrone, A., Henderson, T., Ranasinghe, D., Zakrzewski, V. G., Gao, J., Rega, N., Zheng, G., Liang, W., Hada, M., Ehara, M., Toyota, K., Fukuda, R., Hasegawa, J., Ishida, M., Nakajima, T., Honda, Y., Kitao, O., Nakai, H., Vreven, T., Throssell, K., Montgomery, J. A., Peralta, J. E., Ogliaro, F., Bearpark, M. J., Heyd, J. J., Brothers, E. N., Kudin, K. N., Staroverov, V. N., Keith, T. A., Kobayashi, R., Normand, J., Raghavachari, K., Rendell, A. P., Burant, J. C., Iyengar, S. S., Tomasi, J., Cossi, M., Millam, J. M., Klene, M., Adamo, C., Cammi, R., Ochterski, J. W., Martin, R. L., Morokuma, K., Farkas, O., Foresman, J. B., and Fox, D. J.: Gaussian 16, Revision C.01, [code], 2016.

Fu, X., Hernández, D., Attinson, D. N., Kponee, K. Z., Bartelli, D., Gretz, A. M., Smith, J. N., and Jia, C.: Airborne 2,5-dimethylfuran as a marker to indicate exposure to indoor tobacco and biomass burning smoke, Atmos. Environ., 259, 118 509, https://doi.org/10.1016/j.atmosenv.2021.118509, 2021.

Garmash, O., Rissanen, M. P., Pullinen, I., Schmitt, S., Kausiala, O., Tillmann, R., Zhao, D., Percival, C., Bannan, T. J., Priestley, M., Hallquist, Å. M., Kleist, E., Kiendler-Scharr, A., Hallquist, M., Berndt, T., McFiggans, G., Wildt, J., Mentel, T. F., and Ehn, M.: Multi-generation OH oxidation as a source for highly oxygenated organic molecules from aromatics, Atmos. Chem. Phys., 20, 515–537, https://doi.org/10.5194/acp-20-515-2020, 2020.

Gillespie, D. T.: A general method for numerically simulating the stochastic time evolution of coupled chemical reactions, J. Comput. Phys., 22, 403–434, https://doi.org/10.1016/0021-9991(76)90041-3, 1976.

Gilman, J. B., Lerner, B. M., Kuster, W. C., Goldan, P. D., Warneke, C., Veres, P. R., Roberts, J. M., de Gouw, J. A., Burling, I. R., and Yokelson, R. J.: Biomass burning emissions and potential air quality impacts of volatile organic compounds and other trace gases from fuels common in the US, Atmos. Chem. Phys., 15, 13 915–13 938, https://doi.org/10.5194/acp-15-13915-2015, 2015.

Glowacki, D. R., Liang, C.-H., Morley, C., Pilling, M. J., and Robertson, S. H.: MESMER: an open-source master equation solver for multi-energy well reactions, J. Phys. Chem. A, 116, 9545–9560, https://doi.org/10.1021/jp3051033, 2012.

Guo, H.-T., Tang, Y., Liu, S.-H., Ma, Y., Fang, S., Curran, H. J., and Zhou, C.-W.: Kinetic properties study of H atom abstraction by CH_3O_2 radicals from fuel molecules with different functional groups, J. Phys. Chem. A, 127, 1960–1974, https://doi.org/10.1021/acs.jpca.2c08100, 2023.

Hakala, J. and Donahue, N. M.: Carbonyl oxide stabilization from trans alkene and terpene ozonolysis, J. Phys. Chem. A, 127, 8530–8543, https://doi.org/10.1021/acs.jpca.3c03650, 2023.

Hallquist, M., Wenger, J. C., Baltensperger, U., Rudich, Y., Simpson, D., Claeys, M., Dommen, J., Donahue, N. M., George, C., Goldstein, A. H., Hamilton, J. F., Herrmann, H., Hoffmann, T. I., Iinuma, Y., Jang, M., Jenkin, M. E., Jimenez, J. L., Kiendler-Scharr, A., Maenhaut, W., McFiggans, G., Mentel, T. F., Monod, A., Prévôt, A. S. H., Seinfeld, J. H., Surratt, J. D., Szmigielski, R., and Wildt, J.: The formation, properties and impact of secondary organic aerosol: current and emerging issues, Chemical Society Reviews, 38, 2443–2514, https://doi.org/10.1039/B804226M, 2009.

He, X.-C., Shen, J., Iyer, S., Juuti, P., Zhang, J., Koirala, M., Kytoekari, M. M., Worsnop, D. R., Rissanen, M., Kulmala, M., Maier, N. M., Mikkilä, J., Sipilä, M., and Kangasluoma, J.: Characterisation of gaseous iodine species detection using the multi-scheme chemical ionisation inlet 2 with bromide and nitrate chemical ionisation methods, Atmos. Meas. Tech., 16, 4461–4487, https://doi.org/10.5194/amt-16-4461-2023, 2023.

https://doi.org/10.5194/egusphere-2026-4450
Preprint. Discussion started: 13 August 2026

Hinsberg, W. and Houle, F.: Kinetiscope: a stochastic kinetics simulator, http://hinsberg.net/kinetiscope, [code], last access: 6 February 2026, 2022.

Hippler, H., Troe, J., and Wendelken, H. J.: Collisional deactivation of vibrationally highly excited polyatomic molecules. II. Direct observations for excited toluene, J. Chem. Phys., 78, 6709–6717, https://doi.org/10.1063/1.444670, 1983.

Hoang, A. T., Pandey, A., Huang, Z., Luque, R., Ng, K. H., Papadopoulos, A. M., Chen, W.-H., Rajamohan, S., Hadiyanto, H., Nguyen, X. P., and Pham, V. V.: Catalyst-based synthesis of 2,5-dimethylfuran from carbohydrates as a sustainable biofuel production route, ACS Sustain. Chem. Eng., 10, 3079–3115, https://doi.org/10.1021/acssuschemeng.1c06363, 2022.

Huang, E., Zhong, L., Xue, J., Zhou, X., Liu, S., Che, L., Li, H., Fan, H., Dong, W., and Yang, X.: Conformer-specific infrared spectroscopy of cationic Criegee intermediates *syn*- and *anti*-CH_3CHOO^+, Nat. Commun., 16, 2313, https://doi.org/10.1038/s41467-025-57670-4, 2025.

Hyttinen, N., Kupiainen-Määttä, O., Rissanen, M. P., Muuronen, M., Ehn, M., and Kurten, T.: Modeling the charging of highly oxidized cyclohexene ozonolysis products using nitrate-based chemical ionization, J. Phys. Chem. A, 119, 6339–6345, https://doi.org/10.1021/acs.jpca.5b01818, 2015.

Illmann, N. and Rösgen, V.: O_3 chemistry of 2,5-dimethylfuran: mechanism development, Environ. Sci.: Atmos., 4, 1000–1011, https://doi.org/10.1039/D4EA00045E, 2024.

Iyer, S., Rissanen, M. P., Valiev, R., Barber, V. P., et al.: Molecular mechanism for rapid autoxidation in α-pinene ozonolysis, Nat. Commun., 14, 4398, https://doi.org/10.1038/s41467-023-40051-2, 2023.

Jiang, J., Carter, W. P. L., Cocker, D. R., and Barsanti, K. C.: Development and evaluation of a detailed mechanism for gas-phase atmospheric reactions of furans, ACS Earth Space Chem., 4, 1254–1268, https://doi.org/10.1021/acsearthspacechem.0c00058, 2020.

Jimenez, J. L., Canagaratna, M. R., Donahue, N. M., Prevot, A. S. H., Zhang, Q., Kroll, J. H., DeCarlo, P. F., Allan, J. D., Coe, H., Ng, N. L., Aiken, A. C., Claflin, M. S., Ulbrich, I. M., Grieshop, A. P., Robinson, A. L., Duplissy, J., Smith, J. D., Wilson, K. R., Lanz, V. A., Hueglin, C., Sun, Y. L., Tian, J., Laaksonen, A., Raatikainen, T., Rautiainen, J., Vaattovaara, P., Ehn, M., Kulmala, M., Tomlinson, J. M., Collins, D. R., and Worsnop, D. R.: Evolution of Organic Aerosols in the Atmosphere, Science, 326, 1525–1529, https://doi.org/10.1126/science.1180353, 2009.

Johnson, D. and Marston, G.: The gas-phase ozonolysis of unsaturated volatile organic compounds in the troposphere, Chem. Soc. Rev., 37, 699–716, https://doi.org/10.1039/b704260b, 2008.

Jokinen, T., Sipilä, M., Junninen, H., Ehn, M., Lönn, G., Hakala, J., Petäjä, T., Mauldin, III, R. L., Kulmala, M., and Worsnop, D. R.: Atmospheric sulphuric acid and neutral cluster measurements using CI-APi-TOF, Atmos. Chem. Phys., 12, 4117–4125, https://doi.org/10.5194/acp-12-4117-2012, 2012.

Jokinen, T., Sipilä, M., Richters, S., Kerminen, V.-M., Paasonen, P., Stratmann, F., Worsnop, D., Kulmala, M., Ehn, M., Herrmann, H., and Berndt, T.: Rapid autoxidation forms highly oxidized RO_2 radicals in the atmosphere, Angew. Chem. Int. Ed., 53, 14 596–14 600, https://doi.org/10.1002/anie.201408566, 2014.

Kao, T.-Y., Chung, C.-A., and Lee, Y.-P.: Rate coefficient and branching ratio for the formation of Criegee intermediate *syn*-/*anti*-CH_3CHOO from $CH_3CHI + O_2$ and the self-reaction of *syn*-/*anti*-CH_3CHOO determined with simultaneous IR/UV probes, J. Phys. Chem. A, 128, 9453–9461, https://doi.org/10.1021/acs.jpca.4c06588, 2024.

Koss, A. R., Sekimoto, K., Gilman, J. B., Selimovic, V., Coggon, M. M., Zarzana, K. J., Yuan, B., Lerner, B. M., Brown, S. S., Jimenez, J. L., Krechmer, J., Roberts, J. M., Warneke, C., Yokelson, R. J., and de Gouw, J.: Non-methane organic gas emissions from biomass

https://doi.org/10.5194/egusphere-2026-4450
Preprint. Discussion started: 13 August 2026

burning: identification, quantification, and emission factors from PTR-ToF during the FIREX 2016 laboratory experiment, Atmos. Chem. Phys., 18, 3299–3319, https://doi.org/10.5194/acp-18-3299-2018, 2018.

Kroll, J. H., Donahue, N. M., Cee, V. J., Demerjian, K. L., and Anderson, J. G.: Gas-Phase Ozonolysis of Alkenes: Formation of OH from Anti Carbonyl Oxides, J. Am. Chem. Soc., 124, 8518–8519, https://doi.org/10.1021/ja0266060, 2002.

Lakmuang, C., Kroeger, A. A., and Karton, A.: Criegee intermediate decomposition pathways for the formation of *o*-toluic acid and 2-methylphenylformate, Chem. Phys. Lett., 748, 137 399, https://doi.org/10.1016/j.cplett.2020.137399, 2020.

Li, M., Liu, Y., and Wang, L.: Gas-phase ozonolysis of furans, methylfurans, and dimethylfurans in the atmosphere, Phys. Chem. Chem. Phys., 20, 24 735–24 743, https://doi.org/10.1039/C8CP04947E, 2018.

Li, Y., Wang, Y., Zhang, R. M., He, X., and Xu, X.: Comprehensive theoretical study on four typical intramolecular hydrogen shift reactions of peroxy radicals: multireference character, recommended model chemistry, and kinetics, J. Chem. Theory Comput., 19, 3284–3302, https://doi.org/10.1021/acs.jctc.3c00033, 2023.

Lin, H.-Y., Huang, Y.-H., Wang, X., Bowman, J. M., Nishimura, Y., Witek, H. A., and Lee, Y.-P.: Infrared identification of the Criegee intermediates *syn*- and *anti*-CH_3CHOO, and their distinct conformation-dependent reactivity, Nat. Commun., 6, 7012, https://doi.org/10.1038/ncomms8012, 2015.

Long, B., Bao, J. L., and Truhlar, D. G.: Atmospheric chemistry of Criegee intermediates: unimolecular reactions and reactions with water, J. Am. Chem. Soc., 138, 14 409–14 422, https://doi.org/10.1021/jacs.6b08655, 2016.

Long, B., Bao, J. L., and Truhlar, D. G.: Rapid unimolecular reaction of stabilized Criegee intermediates and implications for atmospheric chemistry, Nat. Commun., 10, 2003, https://doi.org/10.1038/s41467-019-09948-7, 2019.

Luo, Y., Franzon, L., Zhang, J., Sarnela, N., Donahue, N. M., Kurten, T., and Ehn, M.: Gas-phase observations of accretion products from stabilized Criegee intermediates in terpene ozonolysis with two dicarboxylic acids, Atmos. Chem. Phys., 25, 4655–4664, https://doi.org/10.5194/acp-25-4655-2025, 2025.

Matsumoto, J.: Kinetics of the reactions of ozone with 2,5-dimethylfuran and its atmospheric implications, Chem. Lett., 40, 582–583, https://doi.org/10.1246/cl.2011.582, 2011.

Møller, K. H., Otkjær, R. V., Hyttinen, N., Kurten, T., and Kjaergaard, H. G.: Cost-effective implementation of multiconformer transition state theory for peroxy radical hydrogen shift reactions, J. Phys. Chem. A, 120, 10 072–10 087, https://doi.org/10.1021/acs.jpca.6b09370, 2016.

Møller, K. H., Bates, K. H., and Kjaergaard, H. G.: The importance of peroxy radical hydrogen-shift reactions in atmospheric isoprene oxidation, J. Phys. Chem. A, 123, 920–932, https://doi.org/10.1021/acs.jpca.8b10432, 2020.

Newland, M. J., Bryant, D. J., Dunmore, R. E., Bannan, T. J., Acton, W. J. F., Langford, B., Hopkins, J. R., Sherwen, T., Reeves, C. E., Mills, G. P., Baugitte, S. J.-B., Dias-Junior, C. Q., Mobbs, D., Lewis, A. C., Hamilton, J. F., Carpenter, L. J., and Percival, C. J.: Low-NO_x isoprene oxidation in a Sumatran tropical rainforest, Atmos. Chem. Phys., 21, 7755–7771, https://doi.org/10.5194/acp-21-1613-2021, 2021.

Otkjær, R. V., Jakobsen, H. H., Tram, C. M., and Kjaergaard, H. G.: Calculated hydrogen shift rate constants in substituted alkyl peroxy radicals, J. Phys. Chem. A, 122, 8665–8673, https://doi.org/10.1021/acs.jpca.8b07894, 2018.

Peltola, J., Heinonen, P., and Eskola, A.: Direct kinetic measurements of a cyclic Criegee intermediate; unimolecular decomposition of *c*-$(CH_2)_5COO$, J. Phys. Chem. Lett., 15, 5331–5336, https://doi.org/10.1021/acs.jpclett.4c00554, 2024.

https://doi.org/10.5194/egusphere-2026-4450
Preprint. Discussion started: 13 August 2026

Peräkylä, O., Berndt, T., Franzon, L., Hasan, G., Meder, M., Valiev, R. R., Daub, C. D., Varelas, J. G., Geiger, F. M., Thomson, R. J., Rissanen, M., Kurtén, T., and Ehn, M.: Large Gas-Phase Source of Esters and Other Accretion Products in the Atmosphere, ACS Central Science, 9, 1631–1641, https://doi.org/10.1021/acscentsci.3c00473, 2023.

Qian, Y., Zhu, L., Wang, Y., and Lu, X.: Recent progress in the development of biofuel 2,5-dimethylfuran, Renewable Sustainable Energy Rev., 41, 633–646, https://doi.org/10.1016/j.rser.2014.08.085, 2015.

Rissanen, M. P., Kurten, T., Sipilä, M., Thornton, J. A., Kangasluoma, J., Sarnela, N., Junninen, H., Jørgensen, S., Schallhart, S., Kajos, M. K., Taipale, R., Springer, M., Mentel, T. F., Ruuskanen, T., Petäjä, T., Worsnop, D. R., Kjaergaard, H. G., and Ehn, M.: The formation of highly oxidized multifunctional products in the ozonolysis of cyclohexene, J. Am. Chem. Soc., 136, 15 596–15 606, https://doi.org/10.1021/ja507146s, 2014.

Rissanen, M. P., Mikkilä, J., Iyer, S., and Hakala, J.: Multi-scheme chemical ionization inlet (MION) for fast switching of reagent ion chemistry in atmospheric pressure chemical ionization mass spectrometry (CIMS) applications, Atmos. Meas. Tech., 12, 6635–6646, https://doi.org/10.5194/amt-12-6635-2019, 2019.

Román-Leshkov, Y., Barrett, C. J., Liu, Z. Y., and Dumesic, J. A.: Production of dimethylfuran for liquid fuels from biomass-derived carbohydrates, Nature, 447, 982–985, https://doi.org/10.1038/nature05923, 2007.

Romanias, M. N., Coggon, M. M., Al Ali, F., Burkholder, J. B., Dagaut, P., Decker, Z., Warneke, C., Stockwell, C. E., Roberts, J. M., Tomas, A., Houzel, N., Coeur, C., and Brown, S. S.: Emissions and atmospheric chemistry of furanoids from biomass burning: insights from laboratory to atmospheric observations, ACS Earth Space Chem., 8, 857–899, https://doi.org/10.1021/acsearthspacechem.3c00226, 2024.

Sheps, L., Scully, A. M., and Au, K.: UV absorption probing of the conformer-dependent reactivity of a Criegee intermediate CH_3CHOO, Phys. Chem. Chem. Phys., 16, 26 701–26 706, https://doi.org/10.1039/C4CP04408H, 2014.

Taatjes, C. A., Welz, O., Eskola, A. J., Savee, J. D., Scheer, A. M., Shallcross, D. E., Rotavera, B., Lee, E. P. F., Dyke, J. M., Mok, D. K. W., Osborn, D. L., and Percival, C. J.: Direct measurements of conformer-dependent reactivity of the Criegee intermediate CH_3CHOO, Science, 340, 177–180, https://doi.org/10.1126/science.1234689, 2013.

Tajuelo, M., Rodríguez, A., Díaz-de Mera, Y., Aranda, A., Hurley, M. D., and Wallington, T. J.: Secondary organic aerosol formation from SO_2-influenced photooxidation of 2,5-dimethylfuran, Atmos. Environ., 262, 118 613, https://doi.org/10.1016/j.atmosenv.2021.118613, 2021.

Valiev, R. R., Hasan, G., Salo, V.-T., Kubecka, J., and Kurtén, T.: Intersystem Crossings Drive Atmospheric Gas-Phase Dimer Formation, The Journal of Physical Chemistry A, 123, 6112–6123, https://doi.org/10.1021/acs.jpca.9b02559, 2019.

Vereecken, L. and Nozière, B.: H migration in peroxy radicals under atmospheric conditions, Atmos. Chem. Phys., 20, 7429–7458, https://doi.org/10.5194/acp-20-7429-2020, 2020.

Vereecken, L., Müller, J.-F., and Peeters, J.: Low-volatility poly-oxygenates in the OH-initiated atmospheric oxidation of α-pinene: impact of non-traditional peroxyl radical chemistry, Phys. Chem. Chem. Phys., 9, 5241–5248, https://doi.org/10.1039/b708023a, 2007.

Vereecken, L., Rickard, A. R., Newland, M. J., and Bloss, W. J.: Theoretical study of the reactions of Criegee intermediates with ozone, alkylhydroperoxides, and carbon monoxide, Phys. Chem. Chem. Phys., 17, 23 847–23 858, https://doi.org/10.1039/C5CP03862F, 2015.

Vereecken, L., Novelli, A., Kiendler-Scharr, A., and Wahner, A.: Unimolecular and water reactions of oxygenated and unsaturated Criegee intermediates under atmospheric conditions, Phys. Chem. Chem. Phys., 24, 6428–6443, https://doi.org/10.1039/D1CP05877K, 2022.

Watson, N. A. I., Newland, M. J., Nelson, B. S., Rickard, A. R., and Beames, J. M.: Tropospheric alkene ozonolysis chemistry: an extended computational chemistry assessment of structural effects, Environ. Sci.: Adv., 4, 619–647, https://doi.org/10.1039/D4VA00298A, 2025.

Wavefunction, Inc.: Spartan'24, https://www.wavefun.com, [code], 2024.

https://doi.org/10.5194/egusphere-2026-4450
Preprint. Discussion started: 13 August 2026

Werner, H.-J., Knowles, P. J., Knizia, G., Manby, F. R., Schütz, M., et al.: MOLPRO, version 2024.3, a package of *ab initio* programs, https://www.molpro.net, [code], 2024.

Whelan, C. A., Eble, J., Mir, Z. S., Blitz, M. A., Seakins, P. W., Olzmann, M., and Stone, D.: Kinetics of the reactions of hydroxyl radicals with furan and its alkylated derivatives 2-methyl furan and 2,5-dimethyl furan, J. Phys. Chem. A, 124, 7416–7426, https://doi.org/10.1021/acs.jpca.0c06321, 2020.

Yin, C. and Takahashi, K.: How does substitution affect the unimolecular reaction rates of Criegee intermediates?, Phys. Chem. Chem. Phys., 19, 12 075–12 084, https://doi.org/10.1039/C7CP01091E, 2017.

Yu, H., Møller, K. H., Buenconsejo, R. S., Crounse, J. D., Kjaergaard, H. G., and Wennberg, P. O.: Atmospheric autoxidation chemistry of diethyl ether, ACS ES&T Air, 2, 2566–2576, https://doi.org/10.1021/acsestair.5c00204, 2025.

Yuan, Y., Zhao, X., Wang, S., and Wang, L.: Atmospheric oxidation of furan and methyl-substituted furans initiated by hydroxyl radicals, J. Phys. Chem. A, 121, 9306–9319, https://doi.org/10.1021/acs.jpca.7b09741, 2017.